

ABSTRACT

WILSON, DAVID ANDREW. Combined Effects of Dilution and Co-flow on the Stability of Lifted Non-Premixed Gaseous Flames. (Under the direction of Kevin M. Lyons.)

This research documents experiments and analysis of turbulent, lifted, non-premixed diffusion flames in co-flow and with dilution with implications for the development and operation of biogas-fueled combustors. Fuels used in this study were methane and ethylene. The diluent used was nitrogen. General trends were observed in the liftoff and reattachment behavior as affected by dilution of the fuel stream. Initial liftoff velocity was observed to decrease linearly with dilution, while initial lift height behavior was bimodal. Reattachment conditions were similar in overall behavior to liftoff conditions. Co-flow effects were not included in liftoff and reattachment studies. Combined effects of dilution and co-flow were also studied. Stabilization height compared to radial stabilization was found to be bimodal, with behavior differing in the potential core region compared with the far-field region. Dilution was found to decrease the radial stabilization distance, and co-flow tended to increase the radial stabilization distance. However, both effects were minor. The major results involve heat release effects. For given stabilization heights, stabilization velocity was found to decrease with dilution faster than laminar burning velocity with dilution. Stabilization height was also found to increase rapidly with dilution beyond a certain diluent concentration. Flames were also found to taper inward and become more cylindrical in shape as dilution increases. Implications for several flame stabilization theories are discussed. Future work for confirming the results of this research are also discussed.

DEDICATION

To my parents:

Thank you for your love and support over the years.

I could not have made it this far without you.

BIOGRAPHY

David A. Wilson, a lifelong resident of Brevard, North Carolina, was born January 5, 1981 to Carrol and Ruth Wilson. He graduated from Brevard High School in Transylvania County in 1999. Given that David's father is a graduate of North Carolina State University with a Bachelor of Science degree in Mechanical Engineering (1973), David also chose North Carolina State University for his undergraduate education, earning his Bachelor of Science degree in Mechanical Engineering in May 2003. Due to a slumping job market and a desire to further his education, David enrolled in graduate school in August 2003 and began his work in experimental combustion in January 2004. Throughout high school and college, one of David's greatest joys was playing trumpet in a variety of performing ensembles. At North Carolina State, David proudly supported the football and men's and women's basketball teams in both the marching band and varsity bands for all six years of his enrollment.

ACKNOWLEDGMENTS

The author would like to acknowledge Dr. Kevin M. Lyons for providing a stimulating and worthwhile project with “hands off” direction that allowed for maximum creativity in tailoring the project to my interests.

I would also like to express appreciation to Steven Terry for his guidance, assistance, and friendship. With his help in understanding new concepts and in discerning messages from often cryptic data sets proved invaluable.

TABLE OF CONTENTS

List of Figures	vi
List of Tables	viii
1 Introduction	1
1.1 Impetus for Studies in Dilution	1
1.2 Lifted Flame Stability Theories	4
1.2.1 Turbulent Burning Velocity	4
1.2.2 Large Scale Structures Scalar Dissipation and Laminar Flamelets	6
1.2.3 Triple Flames and Streamline Divergence	7
2 Laminar Burning Velocity and Dilution	9
2.1 Experimental Determination of Laminar Burning Velocity	9
2.2 Computational Determination of Laminar Burning Velocity	12
2.3 Laminar Burning Velocity and Dilution	13
3 Modeling of Round Turbulent Jets	15
3.1 Computational Analysis and Associated Difficulties	15
3.2 Analytic Turbulent Jet Model	17
3.2.1 Model Development	18
3.2.2 Model Additions, Modifications, and Implementation	26
3.2.3 Comparison with Published Data	30
4 Lifted Non-Premixed Flames	32
4.1 General Investigation of Behavior of Diluted Flames	33
4.1.1 Experimental Setup	33
4.1.2 Liftoff and Reattachment Results	36
4.1.3 Combined Effects of Co-flow and Dilution	42
4.2 Detailed Study of Ethylene Flames	46
4.2.1 Experimental Setup	47
4.2.2 Results	47
5 Summary	63
5.1 Conclusions	63
5.2 Future Work	67
6 References	69
7 Appendix	72
7.1 Appendix I: CHEMKIN Reaction Mechanism	73
7.2 Appendix II: Lagrangian Jet Model	78

LIST OF FIGURES

Figure 2-1: Bunsen Burner Flame with flow traced by seed particles [29]	10
Figure 2-2: Flame Surfaces Realized by various imaging techniques [28]	11
Figure 2-3: Laminar Burning velocities for ethylene and methane at various equivalence ratios [30]	11
Figure 2-4: Comparison of calculated laminar burning velocity with published experimental data for ethylene	14
Figure 2-5: Stoichiometric Laminar burning velocity for various initial fuel/nitrogen mixtures	14
Figure 3-1: Jet Model Components	19
Figure 4-1: Co-flow Burner	34
Figure 4-2: Co-flow burner configured for basic experiments	35
Figure 4-3: Sighting flame base against ruler	35
Figure 4-4: Initial Jet Velocity Causing Liftoff for various dilutions	36
Figure 4-5: Initial Liftoff Height for various dilutions	37
Figure 4-6: Total Velocity at Stabilization Point for various dilutions	37
Figure 4-7: Axial Velocity at Stabilization Point for various dilutions	38
Figure 4-8: Nondimensional liftoff velocity for various dilutions	38
Figure 4-9: Jet Velocity at Attachment for various dilutions	39
Figure 4-10: Total Velocity at reattachment point for various dilutions	40
Figure 4-11: Axial velocity at attachment point for various dilutions	41
Figure 4-12: Stabilization Point for various initial jet configurations	43
Figure 4-13: Stabilization height and dimensionless radial stabilization location for various jet configurations	43
Figure 4-14: Dimensionless Stabilization location for various jet configurations	44
Figure 4-15: Nondimensional stabilization velocity versus nondimensional stabilization height	44
Figure 4-16: Camera-averaged image of methane flame	48
Figure 4-17: Ethylene Flame (low lift height) at increasing dilution levels ($U_a = 0$ m/s)	50
Figure 4-18: Ethylene Flame (high lift height) at increasing dilution levels ($U_a = 0$ m/s)	51
Figure 4-19: Ethylene Flame (low lift height) at increasing dilution levels ($U_a = 0.33$ m/s)	52
Figure 4-20: Ethylene Flame (high lift height) at increasing dilution levels ($U_a = 0.33$ m/s)	53
Figure 4-21: Ethylene Flame (low lift height) at increasing dilution levels ($U_a = 0.67$ m/s)	54

Figure 4-22: Ethylene Flame (high lift height) at increasing dilution levels ($U_a = 0.67$ m/s)	55
Figure 4-23: Ethylene Flame (low lift height) at increasing dilution levels ($U_a = 1.05$ m/s)	56
Figure 4-24: Ethylene Flame (high lift height) at increasing dilution levels ($U_a = 1.05$ m/s)	57
Figure 4-25: Dimensionless Radial Stabilization versus Axial Stabilization	58
Figure 4-26: Dimensionless Radial Stabilization versus Dimensionless Axial Stabilization.	58
Figure 4-27: Potential Core Length versus Jet Velocity Ratio	59
Figure 4-28: Initial Jet Velocity for various lift heights, co-flows, and dilutions	60
Figure 4-29: Nondimensional stabilization velocity versus lift height.....	60

LIST OF TABLES

Table 1-1: Typical Natural Gas Composition [1]	2
Table 1-2: Typical Biogas Composition [2]	2
Table 3-1: Watson Data for Methane Stabilization	31
Table 3-2: Model Predicted Quantities for Watson Data.....	31
Table 4-1: Flow Parameters for Images.....	49

1 Introduction

Combustion processes are everywhere in the world around us. From the engines that power our automobiles to the boilers that provide much of our electrical power to the small burners that heat many homes and cook our food, our lives depend on combustion. Combustion brought early man out of the cave and gave him the ability to make metal tools; combustion will continue to be a major force in the future of mankind.

While discovering how to make fire was sufficient understanding of combustion for much of man's history (both recorded and prehistory), more recent changes in the economics and politics of the world have forced man to develop a more complete understanding of the nature of fire and combustion processes. Such studies are motivated to find ways to make more efficient use of nonrenewable fossil resources, take advantage of renewable fuel sources previously not considered, and reduce the pollution levels from whatever fuel source is ultimately utilized.

1.1 Impetus for Studies in Dilution

The goal of shifting dependence away from nonrenewable resources to renewable resources is the principle impetus for one of the pillars of this study—the effects of dilution on flame stability. One may ask, “What connections do dilution and flame stability have with renewable resources?” The flame stability issue will be addressed shortly, but first the issue of dilution.

Table 1-1: Typical Natural Gas Composition [1]

Component	Typical Analysis (%)
Methane	87-96
Ethane	1.8-5.1
Propane	0.1-1.5
iso-Butane	0.01 – 0.3
n-Butane	0.01 – 0.3
iso-Pentane	< 0.14
n-Pentane	<0.04
Hexanes and Heavier Hydrocarbons	< 0.06
Nitrogen	1.3-5.6
Carbon Dioxide	0.1-1.0
Oxygen	0.01-0.1
Hydrogen	< 0.02

Table 1-2: Typical Biogas Composition [2]

Component	Typical Analysis (%)
Methane	50-60
Carbon Dioxide	38-48
Trace Components	2
Trace Components	
Hydrogen	Halo carbons
Hydrogen Sulfide	Volatile Organic Carbons

Table 1-2 lists the typical makeup of biogas produced from landfills or digestion processes (aerobic or anaerobic), and Table 1-1 lists the typical composition of natural gas. Biogas and natural gas do have certain similarities—they both are composed mainly of methane, and they both have inert gasses mixed in. However, the similarities stop here. Unlike natural gas which is almost all methane, biogas is almost evenly composed of methane and carbon dioxide. The major difference between natural gas and biogas from a usage standpoint is the heating value. Natural gas has a typical heating value of 39.2 MJ / m³

[1] and biogas is $23.3 \text{ MJ} / \text{m}^3$ [3]. This means that to achieve the same thermal output a burner must flow 68 percent more biogas (by volume). This increase in flow rate brings us back to the first part of our question—flame stability relating to dilution.

Terry [4], in his work on flame hysteresis, describes several implications of flame stability in practical combustors. Among the effects described are flame liftoff, reattachment, blowout, and blowoff of attached flames. Flame liftoff is when flow conditions exist such that the flame cannot stabilize at the burner and instead stabilizes at some point downstream of the burner. Conversely, reattachment is the phenomenon whereby the flow conditions permit a lifted flame to propagate upstream and reattach to the burner. Blowout and blowoff are related to extinction of the flame. Blowout occurs when a lifted flame, for some reason or another, can no longer stabilize downstream of the burner and subsequently extinguishes. Blowoff occurs when an attached flame lifts off the burner and is unable to stabilize downstream and subsequently extinguishes. With the increased flow rates associated with burning biogas, one could postulate that liftoff and blowout would become more of an issue than with natural gas. Also, dilution may have other effects on flame stability, thereby complicating the situation further. Thus, a thorough understanding of the nature of flame stability coupled with dilution is vital to improving the design and operation of biogas-fueled combustors.

1.2 Lifted Flame Stability Theories

The area in combustion research that deals with the stabilization of turbulent lifted flames is replete with theories. Many of these theories contradict at times, and most best describe one flow regime or another. In short, “The Theory” that will accurately describe the entire situation still remains to be formulated.

Until “The Theory” is formulated, work in the area will undoubtedly continue following a multitude of directions, some fruitful, others not. To this end, the following factions have been identified by the author in an effort to classify the work, completed or in progress, in the field of turbulent lifted flame stabilization:

- Turbulent Burning Velocity
- Large Scale Structures, Scalar Dissipation, and Laminar Flamelets
- Triple Flames and Streamline Divergence

1.2.1 Turbulent Burning Velocity

Many theories have emerged for describing the stabilization of lifted diffusion flames. One of the earliest theories was developed by Vanquickenborne and Van Tiggelin [5]. They theorized that the fuel from a jet and oxidizer from the ambient air are completely premixed at the base of the flame. Also, both assert that the flame “sits” at a location where the turbulent burning velocity equals the velocity of the oncoming fuel/oxidizer jet. While it has been difficult to develop exact relations for the turbulent burning velocity, it can be estimated as being approximately three times larger than the laminar burning velocity for the same fuel/oxidizer system. This theory has been corroborated to some extent by the work of

Eickhoff et al. [6]. In their study of conditions around the flame base, they found a region comprised of 40 to 50 percent fuel. Such a mixture would tend to react quickly and would permit the flame to stabilize against the oncoming flow.

In an effort to correlate turbulent burning velocity with known parameters, Kalghatgi [7] performed a series of experiments relating the turbulent flame heights for fuels of various Schmidt numbers, various jet velocities, as well as other variable parameters. The ultimate result was a correlation for turbulent burning velocity based on laminar burning velocity and the square root of the local axial velocity fluctuations. His correlation for the height at which the flame stabilizes is embedded in the following:

$$\frac{hS_L}{v_f} = C_1 \frac{U_m}{S_L} \left(\frac{\rho_0}{\rho_\infty} \right)^{3/2} \quad \mathbf{1-1}$$

When this is simplified for a particular fuel, the following result for the flame height is obtained

$$h = \frac{C_2 U_m \alpha}{S_L^2} \quad \mathbf{1-2}$$

The result of this equation is that the flame height is proportional to the initial velocity of the jet (U_m) and inversely proportional to a characteristic reaction rate (expressed as S_L^2 / α). Indeed, his experiments did prove that liftoff heights did vary linearly for high Reynolds number flows.

Kalghatgi's work was furthered by the efforts of Brown et al. [8] who performed a parametric study with several fuels in a variety of co-flow configurations with flow field velocities calculated with relations developed by Tieszen [9]. They found that turbulent burning velocity was a good indicator of the likely flame stabilization position in the far field

especially near the blowout condition. However, it was found that three times the laminar burning velocity was a better indicator of flame stabilization position in the near field. This near field stabilization velocity recommendation was corroborated by the work of Watson et al. [10] by direct measurements of the flow field around the flame base. Watson also shows that radial velocity components affect stabilization through local extinction.

1.2.2 Large Scale Structures Scalar Dissipation and Laminar Flamelets

Challenges were issued to the idea that the flame stabilizes in a region that is premixed. Peters and Williams [11] expressed a theory whereby hot combustion products and radicals are entrained into the unburned fuel and surrounding oxidizer through the action of vortical structures. After a given amount of time, the vortical structures have cascaded down to the Kolmogorov scale, and molecular diffusion then homogenized the mixture. Reactions then occur along the fuel/oxidizer interface in the form of strained laminar flame sheets. Increasing strain rates upstream of the stabilization point increase thermal diffusion, thereby lowering the reaction zone temperature and preventing the reaction zone from progressing further upstream. This theory was expanded by Broadwell et al. [12], Miake-Lye and Hammer [13], Dahm and Dibble [14], and Pitts [15].

Common throughout the original theory and all extensions is a critical parameter—the ratio of the local mixing time to the chemical reaction time (the Damkholer number). Damkholer numbers for the blowout condition range from 3.9 to 5.6 according to Broadwell et al. Of note is the fact that Dahm and Dibble found that even very small co-flow velocities cause significant changes in blowout behavior. Their conclusion was that local molecular

mixing rates may be the underlying mechanism controlling blowout in turbulent diffusion flames. Studies by Terry et al. [4] tend to confirm this finding.

In the same spirit of disagreement with Vanquickenborne, Byggstyol and Magnussen [16] have introduced their own theory for the stabilization mechanism. Rather than consider strain from large scale flow structures as the extinction mechanism, they focus on the smallest eddies in the flow. However, like Peters and Williams, Byggstyol and Magnussen's model assumes very little premixing occurs before the fuel and oxidizer reach the flame zone some distance downstream from the nozzle exit.

1.2.3 Triple Flames and Streamline Divergence

Other work has been focused on a completely different stabilization model. This model is based on the idea of a triple flame being the stabilization mechanism. The theory, first posed by Phillips [17], suggests that the base of the flame is composed of three regions. There is an outer, fuel-lean premixed wing on the oxidizer side, an inner, fuel-rich premixed wing on the unburned fuel side, and a trailing diffusion wing. The base is located at the triple point where the three wings begin. Flow field features that tend to dictate the structure of the triple flame were investigated by Kioni et al. [18] and Plessing et al. [19]. Their conclusions dictate that fuel mass fraction gradients normal to the direction of flame propagation and variations in equivalence perpendicular to the flow direction combine to cause the formation of the two "wings" (one fuel rich and one fuel lean). Further downstream, diffusion processes reduce the two premixed wings until only a single diffusion wing exists. Muñiz and Mungal [20] have suggested that so-called "leading edge" combustion is actually what is

responsible for the flame stabilization and that such combustion is consistent with the triple flame phenomenon. One important finding is that the velocity of the fuel entering the flame base is relatively low, averaging somewhere between 1.5 and 3 times the laminar burning velocity, which correlates well with many predictions for triple flame numerical models. The models have also been corroborated by Watson et al. [10, 21] for lifted methane flames. However, Watson and Su et al. [22] were unable to locate the rich premixed branch in turbulent flame data. They hypothesize that the rich branch is folded back into the non-premixed branch.

A major aspect of combustion, heat release, has not been directly considered by the stabilization theories presented to this point. The work by Plessing et al. [19] revealed a streamline divergence effect in laminar flames. However, little connection was made between triple flames and heat release. Heat release effects were later studied numerically for laminar flames by Ruetsch et al. [23], Boulanger et al. [24], and Qin et al. [25]. Boulanger et al. found that heat release had a significant impact on stabilization height and that heat release effects permitted the laminar lifted flame to stabilize in a flow field where the local flow velocity was higher than the laminar burning velocity. Qin et al. observed that the triple flame behaved similar to a solid object in the flow field. They postulated that the heat release creates a region of higher pressure inside the flame, and this high pressure region “steers” the flow upstream of the flame front. Using cinema PIV techniques, Upatnieks et al. [26] found evidence of streamline divergence in lifted turbulent diffusion flames, indicating that the effect is not limited to the laminar flow regime.

2 Laminar Burning Velocity and Dilution

In earlier stages of combustion research, flame speed data was considered unnecessary. The belief was that enough was known about combustion conditions to negate any benefit from understanding the rate at which a flame would propagate through combustible mixtures. This situation changed as the combustion community turned its attention to lean burn conditions in internal combustion engines [27]. Since then, the development of many theories on lifted flame stabilization relies on knowing the burning velocity of fuel/oxidizer mixtures. To this end, both experimental and numerical methods have been developed to determine these burning velocities.

2.1 Experimental Determination of Laminar Burning Velocity

Most burning velocity data is generated from Bunsen burner flame shape information. Figure 2-1 shows a typical laminar Bunsen flame where the flow is made visible through the use of seed particles and laser illumination. The laminar burning velocity of the mixture is found based on the cross sectional area of the burner (A_t), velocity of the unburned gasses (V_t), and the surface area of the flame cone (A_f) [28].

$$S_L = V_t \frac{A_t}{A_f} \quad 2-1$$

Although simple in concept, difficulties arise when attempting to determine the flame surface area. Figure 2-2 highlights the different flame surfaces that arise from different

imaging techniques. Each surface yields a different flame area and, thus, a different laminar burning velocity.

Other matters complicate measurements of burning velocity from Bunsen flames. For one, diffusion with the surrounding environment can alter the composition of the combusting mixture. Also, quenching effects due to the burner wall can never be completely eliminated, thus necessitating correction factors in the final data analysis. Finally, the flame itself can act as a lens and distort the optical data. This is because the index of refraction is highly dependent on density of materials, and large changes in density occur across the flame. As a result, in general, Bunsen flame data yields results with accuracy on the order of 20 percent [28].

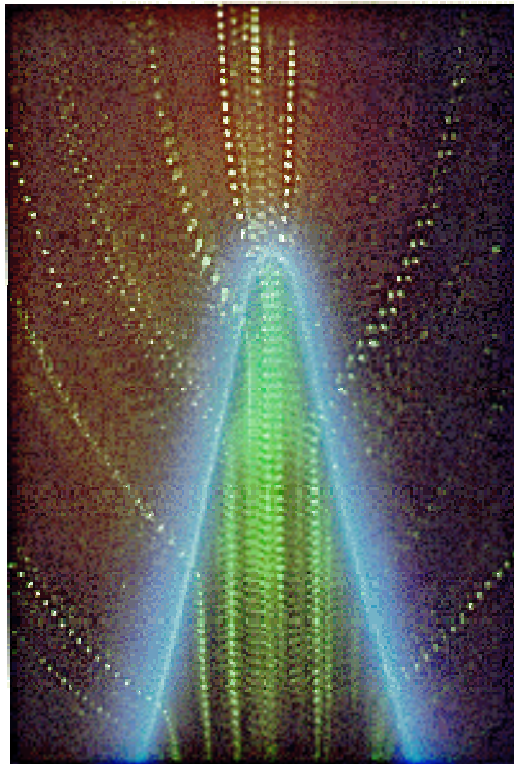


Figure 2-1: Bunsen Burner Flame with flow traced by seed particles [29]

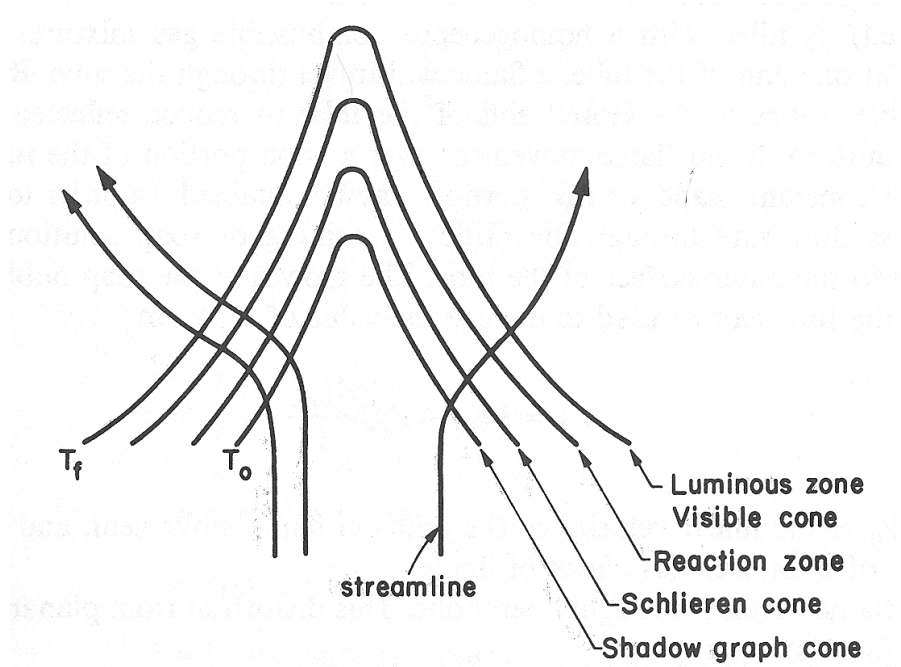


Figure 2-2: Flame Surfaces Realized by various imaging techniques [28]

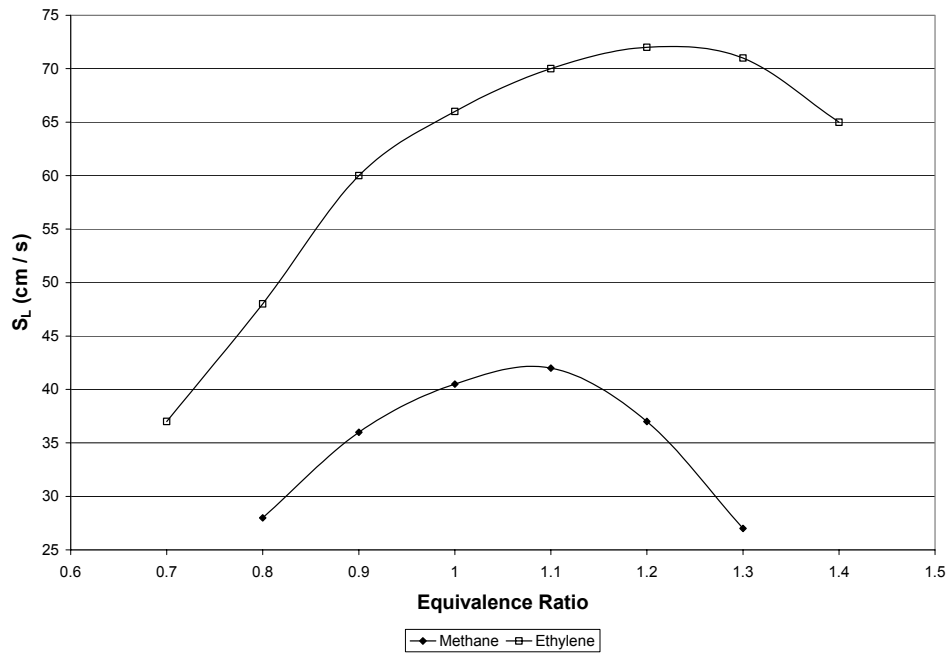


Figure 2-3: Laminar Burning velocities for ethylene and methane at various equivalence ratios [30]

2.2 Computational Determination of Laminar Burning Velocity

With the decrease in cost associated with computational resources in recent years, it is now possible to determine the laminar burning velocity of a mixture based on chemical kinetics and the solution of a set of governing equations. The equations governing the propagation of a quasi-one-dimensional, steady-state, isobaric flame are continuity (2-2), energy (2-3), species (2-4), and state (2-5). Chemical reaction rates are represented in the Arrhenius form (2-6), and transport properties are derived from kinetic theory.

$$\dot{M} = \rho u A \quad 2-2$$

$$\dot{M} \frac{dT}{dx} - \frac{1}{C_p} \frac{d}{dx} \left(\lambda A \frac{dT}{dx} \right) + \frac{A}{C_p} \sum_{k=1}^K \dot{\omega}_k h_k W_k = 0 \quad 2-3$$

$$\dot{M} \frac{dY_k}{dx} + \frac{d}{dx} (\rho A Y_k V_k) - A \dot{\omega}_k W_k = 0 \quad (k = 1, \dots, K_g) \quad 2-4$$

$$\rho = \frac{P \bar{W}}{RT} \quad 2-5$$

$$k_f = AT^\beta \exp\left(\frac{-E_A}{RT}\right) \quad 2-6$$

At this point, all that remains is to solve the equations for a given reaction mechanism. Sandia National Labs developed a suite of programs for accomplishing this task (CHEMKIN). The PREMIX routine in the CHEMKIN suite allows for the solution of both burner-stabilized and freely propagating flames. For determining the laminar burning velocity, the freely propagating model is used.

Many chemical mechanisms have been developed for modeling the combustion of hydrocarbons under a variety of conditions. The one chosen for use in this study was developed by the Center for Energy Research at the University of California, San Diego.

The mechanism was developed to more accurately predict ignition, detonation, and burning rates compared to other available mechanisms (mechanism provided in Appendix I: CHEMKIN Reaction Mechanism). Figure 2-4 gives a comparison of the mechanism-predicted laminar burning velocity for ethylene compared with experimental data from Law, Gibbs and Calcote, and Egolfopoulos et al. (plot produced by mechanism developers). In general, the model results predict published experimental data quite well. The model does over predict the peak burning velocity slightly, and it predicts it at a lower equivalence ratio.

2.3 Laminar Burning Velocity and Dilution

With the aid of CHEMKIN and the light hydrocarbon combustion mechanism previously described, it is possible to determine the effects of diluents on laminar burning velocity. Figure 2-5 depicts the effect of nitrogen dilution on the laminar burning velocities of methane and ethylene. In that scenario, the system is modeled as a mixture of fuel and nitrogen being burned at stoichiometric conditions in standard air (3.76 moles of nitrogen for every mole of oxygen). X_{fuel} represents the mole fraction of fuel in the initial fuel/diluent stream, not the mole fraction of fuel at stoichiometry.

The results in Figure 2-5 illustrate similar trends for both fuels analyzed. Both fuels demonstrate a small reduction in laminar burning velocity for fuel dominant fuel/diluent mixtures. However, for mixtures where the diluent concentration is dominant, the laminar burning velocity decrease is more dramatic. The polynomial trend fits of the two data sets, while unmotivated, will be used in subsequent analyses for determining the role, if any, of laminar burning velocity on lifted turbulent gas flame stabilization.

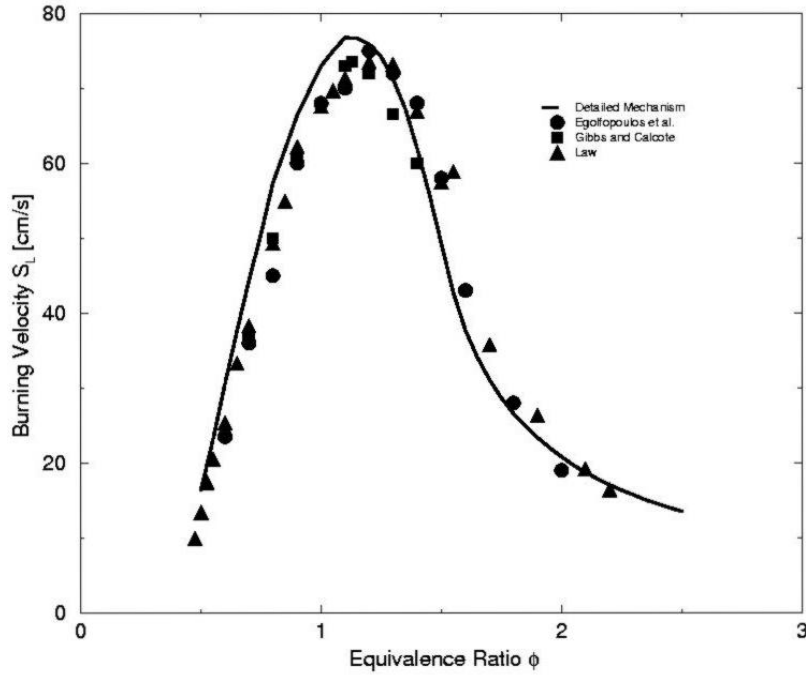


Figure 2-4: Comparison of calculated laminar burning velocity with published experimental data for ethylene¹

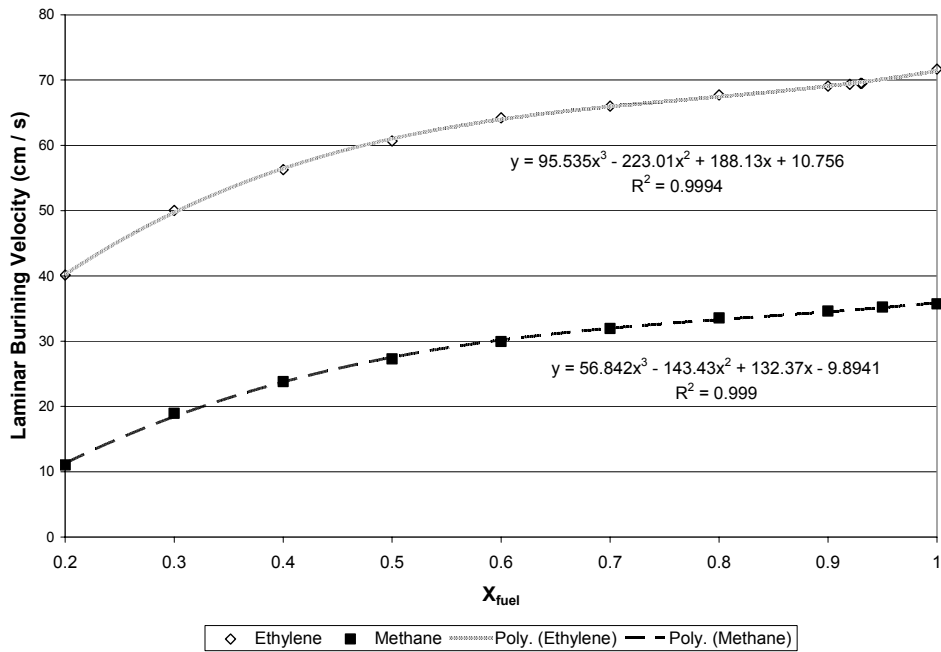


Figure 2-5: Stoichiometric Laminar burning velocity for various initial fuel/nitrogen mixtures

¹ Plot generated by Center for Energy Research, University of California, San Diego

3 Modeling of Round Turbulent Jets

Jets are a class of flows that are particularly important to the study of combustion. This is because most burners, both experimental and industrial, make use of a jet to deliver fuel into a combustion chamber. In the case of non-premixed combustion, the interaction of the fuel stream and oxidizer in the jet structure is responsible for bringing about mixture conditions suitable for combustion. The jet characteristics (velocity, structure sizes and types, etc.) also determine flame characteristics such as flame height, flame shape, and, in the case of lifted flames, lift height. The way the jet entrains surrounding oxidizer and the behavior of the accompanying structures are the subjects of much interest both in the realm of fluid mechanics and combustion science.

3.1 Computational Analysis and Associated Difficulties

Like any other class of fluid flow, the behavior of a jet can be determined by solving the Navier-Stokes equations with the appropriate boundary conditions. Since the focus of this discussion is turbulent, axisymmetric jets, the pertinent equations are continuity (3-1) and axial momentum (3-2). Also, since combustion involves the mixing of fuel and oxidizer, an equation dealing with species concentration is needed. In this case, an equation for tracer-mass conservation (3-3) will be incorporated. These equations in Reynolds-Averaged form are as follows:

$$\rho \frac{\partial u}{\partial x} + \rho \frac{1}{r} \frac{\partial}{\partial r} (rv) = 0 \quad 3-1$$

$$\rho u \frac{\partial u}{\partial x} + \rho v \frac{\partial u}{\partial r} = -\frac{1}{r} \frac{\partial}{\partial r} (r \rho \overline{u'v'}) \quad 3-2$$

$$u \frac{\partial c}{\partial x} + v \frac{\partial c}{\partial r} = -\frac{1}{r} \frac{\partial}{\partial r} (r \overline{v'c'}) \quad 3-3$$

The problem associated with the turbulent, Reynolds-Averaged Navier-Stokes equations (RANS) is that there are more unknowns than equations. The fluctuating velocity and concentration terms (u', v', c') must be modeled in some way, as this information is not captured by the Navier-Stokes equations. The modeling of these fluctuations has been the focus of much effort in the computational fluid dynamics arena. Several models have been developed, each best suited to certain classes of flows and with varying computational expense (Cho and Chung [31], Merci and Dick [32], and Jaw and Chen [33]). However, the axisymmetric jet has posed particular difficulty.

More recent advances in computational power have brought new possibilities to light for computing flows. These methods do not rely on using the Reynolds-Averaged form of the Navier-Stokes equations. Rather, the complete, unsteady, unaveraged Navier-Stokes equations are solved directly. The two methods employed are Direct Numerical Simulation (DNS) and Large Eddy Simulation (LES). Simply, the difference in the two methods is the computational expense involved. With DNS the resolution of the computational grid must be fine enough so that eddies of even the smallest length scale are captured. Typical problems will have a ten decade range in length scales and a six decade range in time scales. However, since all length scales are captured, the quality of the solution, in theory, should be quite good. Even so, the fine grid resolution results in a stiff system of either finite-difference or finite-volume equations. Ultimately, the solution is only as good as the numerical methods used to solve the spatial and temporal portions of the problem. The combination of fine grids

and high-order numerical methods results in an extremely computationally expensive simulation for even the simplest flow conditions. This makes DNS infeasible for engineering calculations. LES is a derivative of DNS that offers DNS-like accuracy but with less computational expense. With LES the grid resolution used is only fine enough to capture the physics of large-scale structures. Effects due to flow structures smaller than the computational grid (known as subgrid structures) are then modeled rather than solved directly. The disadvantage to LES is that the final solution depends on the quality of the subgrid turbulence model employed. However, since the larger-scale structures are responsible for the majority of the mixing involved with combustion, LES offers promise for improving the modeling of turbulent combustion. However, LES is still computationally expensive especially compared to many of the RANS formulations currently favored by individuals dealing with engineering flows.

What is needed is a model for turbulent jets that yields satisfactory results with little computational effort. The best hope would be to develop an analytical solution. Such efforts are being made. The derivation of these models relies on employing some powerful assumptions grounded in empirical evidence.

3.2 Analytic Turbulent Jet Model

In their analysis of turbulent jets and plumes, Chu and Lee [34] discuss the behavior of turbulent jets. Their findings demonstrate that:

- The entrainment and spreading rate of a jet is dominated by large-scale eddies
- Ultimate mixing is carried out by small-scale eddies

- A core of irrotational fluid exists at the jet exit that is not affected by jet diffusion (known as the potential core)
- Initial jet development is dominated by a mixing layer around the potential core
- Beyond the potential core, all jet fluid is mixed with the ambient fluid and the mean flow is fully developed

Based on experimental evidence, Chu and Lee show that the time-averaged axial velocity and tracer concentration profiles are well approximated by the Gaussian distribution (3-4) where the subscript m denotes the peak or centerline value of the function, and b_g is the radial position at which the parameter of the jet being modeled, either axial velocity or concentration, is one-half the magnitude of that at the centerline (also known as the jet half-width).

$$\frac{U}{U_m} = e^{-\left(\frac{r^2}{b_g^2}\right)} \quad 3-4$$

3.2.1 Model Development

In order to calculate the flow field for a jet based on the evidence presented by Chu and Lee, a method is needed to determine the jet spreading parameter b_g at any axial location as well as the centerline velocity (U_m) and concentration (C_m). The spreading parameter is calculated by invoking the Jet Spreading Hypothesis, and the centerline quantities will be developed from conservation of jet momentum.

At this point, it becomes more convenient to discuss the jet properties in terms of “top-hat” representation. In such a representation, the quantity being modeled, either

velocity or concentration, is averaged across a given spatial area (see left side of Figure 3-1). The conversion of top-hat data to the more physically correct Gaussian profiles will be discussed later.

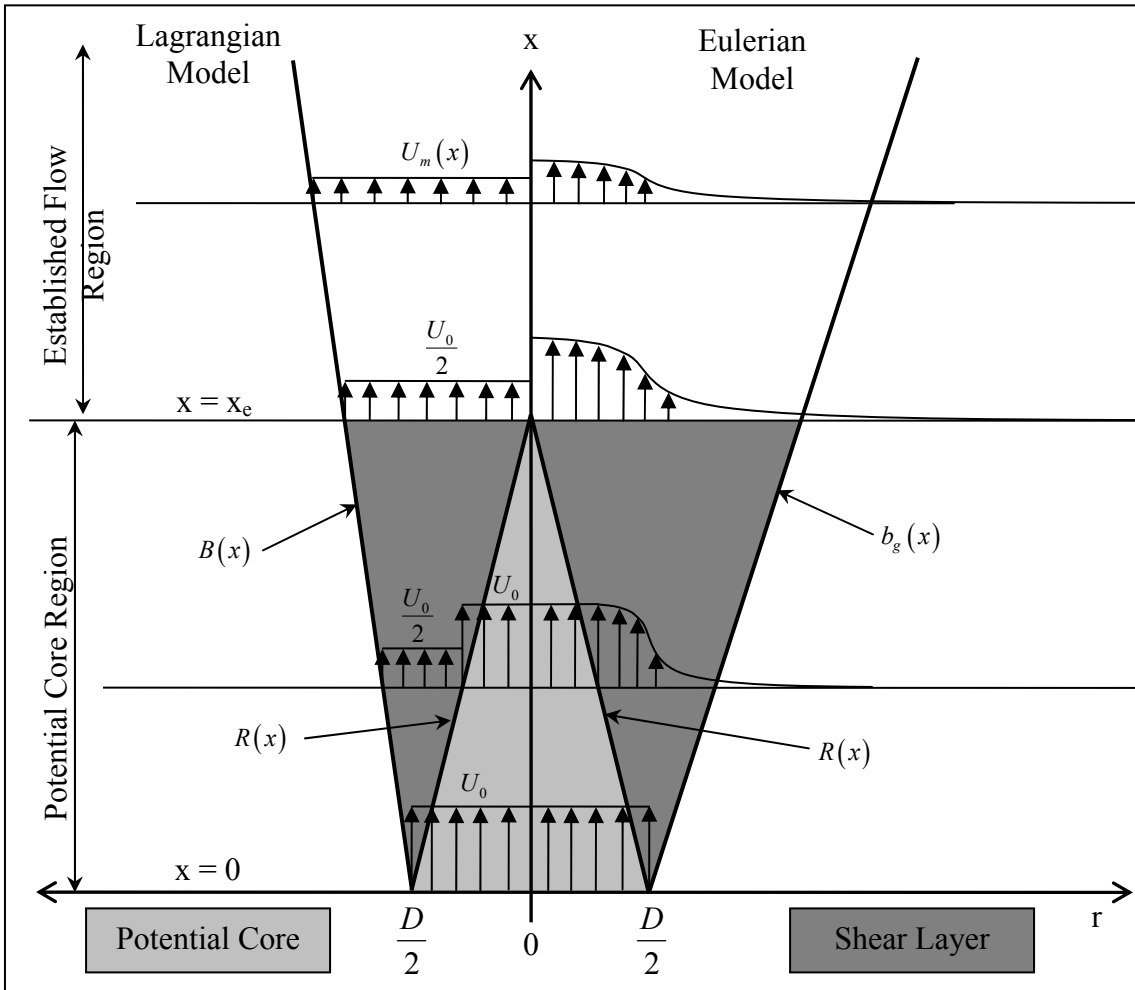


Figure 3-1: Jet Model Components

The jet spreading hypothesis states that the change in width of the shear layer is proportional to the relative velocity between the jet element and its surroundings [34]. This statement applies to the Lagrangian reference frame, a reference frame moving with the dominant eddies. This hypothesis, stated mathematically, yields

$$u \frac{dB}{dx} = \beta u_e \quad 3-5$$

where β is a proportionality constant, u is the characteristic jet velocity, and u_e is the excess velocity of the jet in top-hat representation. The excess velocity is defined as

$$u_e = \begin{cases} 0 & ; U_a = 0 \\ u - U_a & ; U_a > 0 \end{cases} \quad 3-6$$

where U_a is the velocity of the ambient fluid (i.e. co-flowing jet). β is best determined experimentally from jets issuing into stagnant environments because the spreading hypothesis reduces to

$$\frac{dB}{dx} = \beta \quad 3-7$$

After separating variables and integrating, the spreading hypothesis yields

$$B(x) = \beta x + C_1 \quad 3-8$$

where C_1 is the constant resulting from integration. The value for C_1 is determined from the boundary condition at the jet exit (see Figure 3-1).

$$B(0) = \frac{D}{2} \quad 3-9$$

Thus, the spreading parameter for a jet issuing into a stagnant environment is given as

$$B(x) = \beta x + \frac{D}{2} \quad 3-10$$

This equation, when applied to time-averaged experimental data yields

$$\beta = 0.109 \quad 3-11$$

Another of the features of the jet that must be modeled is the decay of the potential core. Experimental evidence suggests that the potential core decays in a more-or-less linear fashion. This decay can be represented as

$$R(x) = \begin{cases} \frac{D}{2} \left(1 - \frac{x}{x_e} \right) & ; \quad x < x_e \\ 0 & ; \quad x \geq x_e \end{cases} \quad 3-12$$

where $R(x)$ is the radius of the potential core at a given downstream position, and x_e is the end of the potential core. To solve for the location of the end of the potential core, the velocity of the mixing layer (region where $R(x) < r < B(x)$) is taken to be the average of the potential core velocity and the ambient fluid velocity.

$$u = \frac{U_0 + U_a}{2} \quad 3-13$$

Next, the spreading hypothesis equation (3-5) is integrated over the potential core region to find the jet width at the end of the potential core.

$$\int_{x=0}^{x=x_e} d(B-R) = \int_0^{x_e} \beta_s \frac{U_0 - U_a}{U_0 + U_a}$$

$$B(x_e) - B(0) - R(x_e) + R(0) = \beta_s \frac{U_0 - U_a}{U_0 + U_a} x_e$$

With the width of the jet known at the end of the potential core, conservation of excess momentum for the jet is examined.

$$\begin{aligned}
 M_{e,0} &= M_{e,x_e} \\
 2\pi \int_0^{D/2} U_0 (U_0 - U_a) r dr &= 2\pi \int_0^R U_0 (U_0 - U_a) r dr + 2\pi \int_R^B uu_e r dr \\
 \frac{D^2}{4} U_0 (U_0 - U_a) &= R^2 U_0 (U_0 - U_a) + (B^2 - R^2) \frac{U_0 + U_a}{2} \frac{U_0 - U_a}{2} \\
 \left(\frac{D^2}{4} - R^2 \right) U_0 (U_0 - U_a) &= \frac{B^2 - R^2}{4} (U_0^2 - U_a^2) \tag{3-14}
 \end{aligned}$$

At the end of the potential core ($x = x_e$), $R(x_e) = 0$. $B(x_e)$ is given by 3-15 and the potential core length is give by 3-16.

$$\begin{aligned}
 \frac{D^2}{4} U_0 (U_0 - U_a) &= \frac{B(x_e)^2}{4} (U_0^2 - U_a^2) \\
 \frac{B(x_e)}{D} &= \sqrt{\frac{U_0}{U_0 + U_a}} \\
 B(x_e) &= \beta \frac{U_0 - U_a}{U_0 + U_a} x_e \tag{3-15}
 \end{aligned}$$

$$\begin{aligned}
 \frac{\beta U_0 - U_a}{D U_0 + U_a} x_e &= \sqrt{\frac{U_0}{U_0 + U_a}} \\
 x_e &= \sqrt{\frac{U_0}{U_0 + U_a}} \left(\frac{\beta U_0 - U_a}{D U_0 + U_a} \right)^{-1} \tag{3-16}
 \end{aligned}$$

For the no co-flow case, this model predicts a potential core length of 6.5*D. This is in agreement with the potential core length of 6.2*D reported by Chu and Lee from their experiments.

At this point, all the major features of the jet are either known or are modeled based on known quantities except for one—the outer edge of the jet. This is determined by solving

the spreading hypothesis equation (3-5). However, a relation is needed for the shear layer velocity u that appears in the equation. This quantity, like others in the model, is found from conservation of excess momentum.

$$2\pi \int_0^{D/2} U_0 (U_0 - U_a) r dr = 2\pi \int_0^R U_0 (U_0 - U_a) r dr + 2\pi \int_R^B u u_e r dr \quad 3-17$$

This equation is integrated and solved for u . The result is given by the following:

$$u = -\frac{U_a}{2} + \frac{\sqrt{U_a^2 + 4\gamma}}{2} \quad 3-18$$

$$\gamma = \frac{U_0 (U_0 - U_a) (D^2 - 4R^2)}{4(B^2 - R^2)}$$

The jet width can now be found by integrating the system of equations represented by 3-5 and 3-18. Due to the nonlinear nature of the differential equation for the co-flow case, the system must be integrated numerically. Such integration was done with an adaptive step RKF45 routine [35]. Also, rather than force the routine to end at the desired axial location (x value), the routine was allowed to overshoot the required endpoint (integrate further downstream). The required endpoint was then interpolated by a three-point Legendre interpolation technique [36].

Top-hat profiles are sufficient for determining jet trends, but they do not model the behavior of the velocity field well. Chu and Lee, among others, have found through experiments that the time-averaged profiles found in real jets are Gaussian in nature. To convert the flow data from top-hat to Gaussian, conservation of excess momentum (3-20) and conservation of excess volume flux (3-19) are applied to the two profile classes.

$$Q_e = \int u_e dA \quad 3-19$$

$$M_e = \int uu_e dA \quad 3-20$$

$$M_{e,TH} = M_{e,g}$$

$$2\pi \int_0^B U(U + U_a) r dr = 2\pi \int_0^\infty U_m e^{\left(-\frac{r^2}{b^2}\right)} \left(U_m e^{\left(-\frac{r^2}{b^2}\right)} + U_a \right) r dr$$

$$U(U + U_a)B = \frac{1}{2}U_m^2 b^2 + U_m U_a b^2 \quad 3-21$$

$$Q_{e,TH} = Q_{e,g}$$

$$2\pi \int_0^B U r dr = 2\pi \int_0^\infty U_m e^{\left(-\frac{r^2}{b^2}\right)} r dr$$

$$U \frac{B^2}{2} = U_m \frac{b^2}{2}$$

$$U = U_m \frac{b^2}{B^2} \quad 3-22$$

Solving the system of equations represented by 3-21 and 3-22, the following relations comparing top-hat parameters to Gaussian parameters can be found.

$$B = b\sqrt{2}$$

$$U = \frac{U_g}{2} \quad 3-23$$

With the relations given in 3.23, any analysis performed in top-hat representation can be converted to the more physically correct Gaussian representation.

The following equation describes the axial velocity at any point (r, x) in the flow field (see 3-24). Note: U , R , and B are the top-hat quantities. All necessary conversions are already included so the top-hat quantities yield the appropriate Gaussian quantities.

$$u(r, x) = \begin{cases} 2(U_0 - U_a) \exp\left(-\frac{2(r-R)^2}{B^2}\right) + U_a & ; x \leq x_e, r > R \\ U_0 & ; x \leq x_e, r \leq R \\ 2U \exp\left(-\frac{2r^2}{B^2}\right) + U_a & ; x > x_e, r \geq 0 \end{cases} \quad 3-24$$

The final component that needs to be modeled is the tracer mass concentration. From their experiments, Chu and Lee determined that the time-averaged concentration profiles in a turbulent jet (with or without co-flow) were Gaussian in nature and that the spread term in the Gaussian function was simply a scalar multiple of the spread term in the velocity profile Gaussian function (3-25). Chu and Lee determined the value of this scalar to be $\lambda = 1.2$.

$$b_c = \lambda b \quad 3-25$$

The behavior of the tracer mass concentration in the potential core region of the jet was also found to closely mimic the behavior of the velocity profile. The tracer mass concentration was constant in the potential core and decayed in a Gaussian manner outside the potential core. Beyond the potential core, the action of large-scale structures caused dilution of the tracer mass at the centerline of the jet. This dilution is modeled by looking at conservation of tracer mass. The initial tracer mass flux is given in 3-26, where C_0 is the initial mass fraction of tracer in the jet stream.

$$\Gamma_0 = \frac{\pi D^2}{4} C_0 U_0 \quad 3-26$$

Equating the tracer mass flux at some downstream location to the initial tracer mass flux yields the following:

$$\begin{aligned} \Gamma_0 &= \Gamma_{x>x_e} \\ \frac{\pi D^2}{4} C_0 U_0 &= 2\pi \int_0^\infty C_g \exp\left(-\left(\frac{r}{\lambda b}\right)^2\right) \left[U_g \exp\left(-\left(\frac{r}{b}\right)^2\right) + U_a \right] r dr \\ \frac{D^2}{4} C_0 U_0 &= \lambda^2 b^2 C_g \left(U_a + \frac{U_g}{1+\lambda^2} \right) \end{aligned}$$

$$C_g = \frac{D^2 C_0 U_0}{4 \lambda^2 b^2} \left(U_a + \frac{U_g}{1+\lambda^2} \right)^{-1} \quad 3-27$$

The following equation describes the tracer mass concentration at any point (r, x) in the flow field (3-28). Note: R and B are the top-hat quantities. All necessary conversions are already included so the top-hat quantities yield the appropriate Gaussian quantities.

$$C(r, x) = \begin{cases} C_0 \exp\left(-\frac{2(r-R)^2}{\lambda^2(B-R)^2}\right) & ; \quad x \leq x_e, \quad r > R \\ C_0 & ; \quad x \leq x_e, \quad r \leq R \\ C_g \exp\left(-\frac{2r^2}{\lambda^2 B^2}\right) & ; \quad x > x_e, \quad r \geq 0 \end{cases} \quad 3-28$$

3.2.2 Model Additions, Modifications, and Implementation

The model proposed by Chu and Lee models only the time-averaged axial velocity field for the axisymmetric jet. Also of interest is the time-averaged radial velocity field.

This is found by solving the continuity equation (3-1) for v . Assuming a constant density for the flow field, the continuity equation reduces to

$$\frac{\partial u}{\partial x} + \frac{1}{r} \frac{\partial}{\partial r}(rv) = 0 \quad 3-29$$

However, this is not a simple procedure. The first term in (3-29) is not known completely analytically because the spreading term for the jet was integrated numerically. Even so, numerous finite difference techniques abound for finding a numerical value for this derivative from a known axial velocity field. However, the first term is also a function of the radial position in the flow field. It quickly becomes apparent that this equation cannot be integrated analytically.

The solution chosen in this case was to discretize the equation with backwards finite differences and solve the resulting system of linear equations with matrix methods. The discretized form of 3-29 is given below (superscript i indicates node number in the radial direction, and superscript j indicates node number in the axial direction).

$$\begin{aligned} v + r \frac{\partial v}{\partial r} &= -r \frac{\partial u}{\partial z} \\ v^{i,j} + r^i \left(\frac{v^{i,j} - v^{i-1,j}}{\Delta r} \right) &= -r^i \left(\frac{u^{i,j} - u^{i,j-1}}{\Delta x} \right) \\ v^{i,j} \left(1 + \frac{r^i}{\Delta r} \right) + v^{i-1,j} \left(-\frac{r^i}{\Delta r} \right) &= -r^i \left(\frac{u^{i,j} - u^{i,j-1}}{\Delta x} \right) \end{aligned} \quad 3-30$$

Since the partial differential equation is first order, only one boundary condition needs to be specified. Since the jet is axisymmetric, the boundary condition that naturally appears is

$$v(r=0) = 0 \quad 3-31$$

Based on 3-30 and the boundary condition specified by 3-31, the finite difference mesh can be represented as

$$\begin{bmatrix} 1 & 0 & & & & \\ A^2 & B^2 & 0 & & & \\ & \ddots & \ddots & \ddots & & \\ & & A^{n-1} & B^{n-1} & 0 & \\ & & & A^n & B^n & \end{bmatrix} \begin{bmatrix} v^1 \\ v^2 \\ \vdots \\ v^{n-1} \\ v^n \end{bmatrix} = \begin{bmatrix} 0 \\ F^2 \\ \vdots \\ F^{n-1} \\ F^n \end{bmatrix} \quad 3-32$$

where

$$A^i = -\frac{r^i}{\Delta r} \quad 3-33$$

$$B^i = 1 + \frac{r^i}{\Delta r} \quad 3-34$$

$$F^i = -r^i \left(\frac{u^{i,j} - u^{i,j-1}}{\Delta x} \right) \quad 3-35$$

Numerous methods exist for solving diagonally-dominant matrix equations. The one chosen here is known as Thomas's Algorithm. While developed for tridiagonal systems, it is equally capable of solving bidiagonal systems. The step sizes for the finite differences (Δr and Δx) were reduced until a desired threshold of accuracy was achieved (too small a step size is computationally expensive and too large a step size leads to large errors on the finite differences).

One other modification made to Chu and Lee's model concerns the conversion factors used to convert the top-hat data to the more realistic Gaussian profiles (3.23). The derivation of these constant conversion factors does not take into account the effect of the irrotational fluid in the potential core region. This is especially evident where the jet exits the nozzle ($x = 0$). At that point, the velocity profile should be a pure top-hat. However, the fixed

conversion factors cause the velocity profile to spread at the jet exit. What is needed is a relation for the conversion factors in the potential core region.

To develop their conversion factors, Chu and Lee looked at conservation of jet volume flux and conservation of excess momentum. (Note: even though excess momentum flux is the only one of these two quantities that is truly conserved in the jet, the two quantities should be the same regardless of the velocity profile formulation). In this case, the region of interest is the shear layer that forms between the ambient fluid and the potential core. Once the potential core dissipates, this shear layer makes up the entire jet. Therefore, the volume flux and excess momentum for the potential core region are as follows:

$$\begin{aligned}
 Q_{TH} &= Q_{Gaussian} \\
 2\pi \int_R^B u r dr &= 2\pi \int_R^\infty U_g \exp\left(-\frac{(r-R)^2}{b_g^2}\right) r dr \\
 (B^2 - R^2)u &= U_g b_b (R\sqrt{\pi} + b_g)
 \end{aligned} \tag{3-36}$$

$$\begin{aligned}
 M_{e,TH} &= M_{e,Gaussian} \\
 2\pi \int_R^B u u_e r dr &= 2\pi \int_R^\infty \left(U_g^2 \exp\left(-\frac{(r-R)^2}{b_g^2}\right) - U_g U_a \exp\left(-\frac{(r-R)^2}{b_g^2}\right) \right) r dr \\
 u(u - U_a)(B^2 - R^2) &= \frac{U_g b_g}{2} \left[b_g (U_g - 2U_a) + (U_g R\sqrt{2\pi} - 2U_a R\sqrt{\pi}) \right]
 \end{aligned} \tag{3-37}$$

Equations 3-36 and 3-37 represent the system of equations that are to be solved for b_g and U_g . Solving 3-36 for U_g yields the following:

$$U_g = \frac{(B^2 - R^2)u}{b_b (R\sqrt{\pi} + b_g)} \tag{3-38}$$

Substituting 3-38 for U_g in 3-37 yields

$$b_g = \frac{\lambda^{1/3}}{6} - \frac{6\kappa}{\lambda^{1/3}} - \frac{2R\sqrt{\pi}}{3} \quad 3-39$$

$$\kappa = \frac{\pi R^2}{9} + \frac{1}{6}(R^2 - B^2) \quad 3-40$$

$$\lambda = 8R^3\pi^{3/2} - (B^2 - R^2)(36\sqrt{\pi} - 54R\sqrt{2\pi}) + 6\sqrt{\phi} \quad 3-41$$

$$\begin{aligned} \phi = -6(B^2 - R^2) & \left[B^4 - R^2 B^2 (31\pi - 2 + 18\pi\sqrt{2}) + 31\pi R^2 \right. \\ & \left. - R^4 (4\pi^2\sqrt{2} - 1 - 4\pi^2 + 18\pi\sqrt{2}) \right] \end{aligned} \quad 3-42$$

This model, while analytic, is not simple to evaluate as models proposed by others [9]. To utilize this model, the various components have been built into FORTRAN subroutines, many of which can be called independently. Complete FOTRTAN code is presented in Appendix II: Lagrangian Jet Model.

3.2.3 Comparison with Published Data

A model is only useful if the results it predicts are accurate. The goal in developing this model was to be able to find the velocity at a point that would be specified by a downstream location and a known concentration (the stoichiometric mass fraction for a given fuel). Watson [37] published data for the stabilization point for a lifted turbulent methane flame for several flow conditions all with a 5mm diameter nozzle. His data is listed in Table 3-1. For comparison purposes, the predicted radial stabilization distance and axial, radial, and total velocities are listed in Table 3-2 (estimated quantities denoted with *)

Table 3-1: Watson Data for Methane Stabilization

U_0	U_a	x	r	U
m/s	m/s	m	m	m/s
15.8	0.13	0.0293	0.0072	1.06
21.2	0.13	0.0485	0.0093	1.35
27.5	0.19	0.0751	0.0120	1.73

Table 3-2: Model Predicted Quantities for Watson Data

U_0	U_a	x	r^*	U^*	r error	U error
m/s	m/s	m	m	m/s	%	%
15.8	0.13	0.0293	0.0073	0.63	1.4	41
21.2	0.13	0.0485	0.0092	0.92	1.1	32
27.5	0.19	0.0751	0.0118	1.25	1.7	28

As seen in Table 3-2, the prediction of the radial stabilization point is quite good (two percent or less error over the range of stabilization points tested). However, the model tends to under predict the axial velocity at the stabilization point. Model deficiencies may not be the entire cause of such large discrepancies. The Watson data is based on examining the actual velocity field that coincides with the location of the CH radical signature in the methane flame. The elevated temperatures present in the region of CH radical production would lower the local density of the flow. This drop in density would cause a substantial increase in velocity which is necessary to maintain the continuity condition. Cold-flow velocimetry data is needed to resolve this discrepancy since the model developed by Chu and Lee does not take density variations into consideration.

4 Lifted Non-Premixed Flames

Lifted non-premixed flames serve a variety of purposes in industrial and commercial environments. One specific example of a lifted gaseous non-premixed flame is that in a commercial steam boiler. The lifted flame reduces heat transfer into the actual burner. A burner-stabilized flame transfers a large amount of heat into the burner, thereby necessitating expensive temperature-resistant materials (ceramics, etc.). With a lifted flame, the burner can be constructed from ordinary metals, hence simplifying manufacturing and material costs associated with the boiler.

The recent increased interests in the use of biofuels and waste gas recovery have raised questions about the behavior of flames in diluted fuels. This is because many biogases are upwards of 40 percent inert. These inert gasses reduce the amount of heat produced per unit of fuel, and some may even interfere (or possibly improve) certain aspects of the chemistry involved in the flame structure.

Aside from improving our understanding of how biofuels may potentially perform in industrial burners, studies in dilution also affords the opportunity to investigate many of the proposed lifted flame stabilization mechanisms that rely heavily on heat release. Inert diluents, as previously stated, reduce the heat production per unit of fuel. This is done in two principal ways: 1) lower combustible species concentration in the fuel stream, and 2) absorption of heat evolved from combustion. These methods of reducing heat produced, while simple, may have drastic impacts on flame stability if flame stabilization is as closely linked to heat release as some theorize. However, if the stabilization is less dependent on heat release, then little difference should be observed in the stabilization of a diluted flame compared to an undiluted flame.

With the goal in mind of trying to determine the effect of heat release on flame stability, the choice of fuel becomes paramount. While the largest flammable constituent in biogas is methane, methane has a relatively low heat production rate per unit of fuel. To obtain better resolution on the effects of heat release, it would be better to start with a fuel with a higher heat production rate per unit of fuel. A higher heat rate fuel allows for studying a larger range of dilution. This led to choosing ethylene as the fuel for the majority of the research.

4.1 General Investigation of Behavior of Diluted Flames

The first set of experiments conducted in this study was aimed at exploring general trends in the behavior of diluted flames. The effects of dilution on liftoff height, jet velocity needed to induce liftoff, conditions needed to induce reattachment, and conditions needed to cause blowout were all of interest. The effect of dilution coupled with co-flow was also of interest.

4.1.1 Experimental Setup

Since the overall goal of these experiments was to develop a qualitative sense for the behavior of diluted flames, faster but less-precise methods were used to collect data on various parameters. Fuel and diluent flow rates were controlled and measured with ball rotameters (0 to 50 SLPM range), with one for the fuel and one for the diluent. Co-flow velocity was measured prior to each run at several locations in the flow field with a hot-wire

anemometer. Finally, flame lift heights were measured by sighting the bottommost portion of the flame against a ruler affixed to the burner (see Figure 3-2 and Figure 3-3).

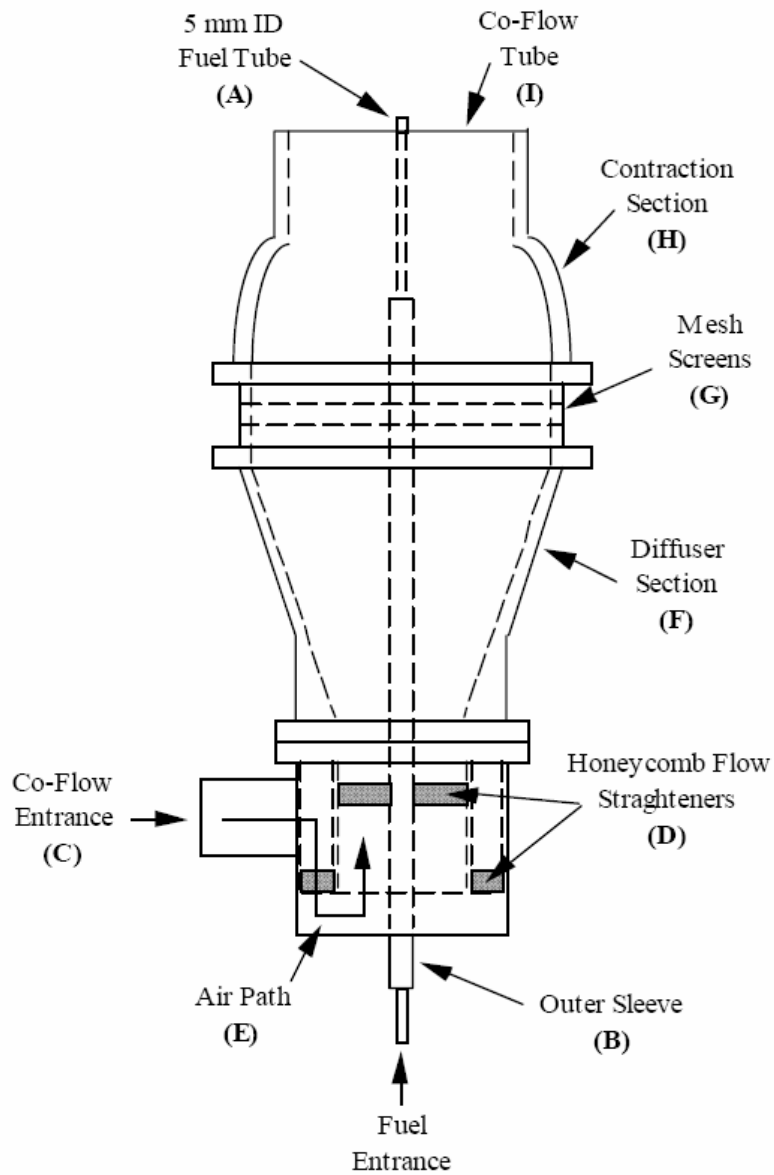


Figure 4-1: Co-flow Burner



Figure 4-2: Co-flow burner configured for basic experiments

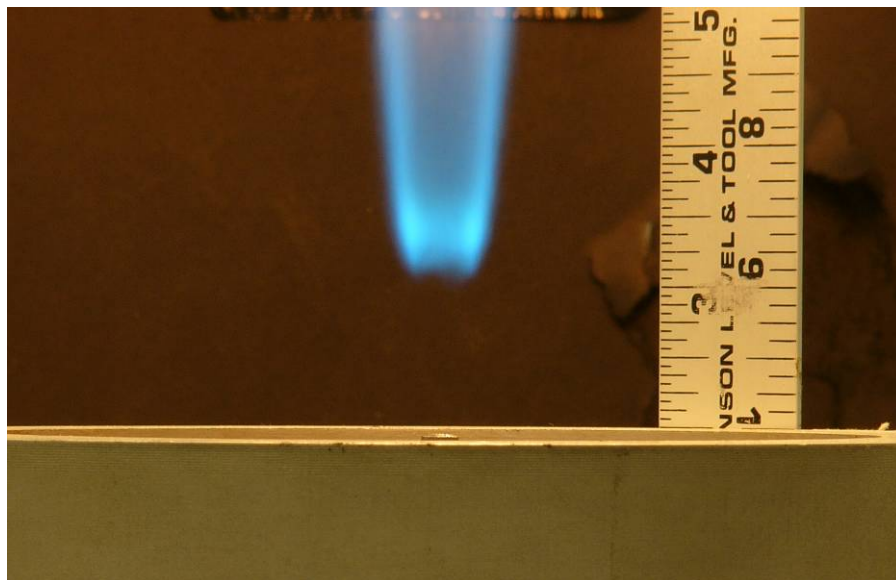


Figure 4-3: Sighting flame base against ruler

4.1.2 Liftoff and Reattachment Results

The first effect of dilution on flame stability that was studied was the effect on initial liftoff and reattachment. The two fuels studied were methane and ethylene, and the diluent used was nitrogen. Two sizes of burners were also used (“small” was 2.2 mm and “large” was 3.6 mm). Flow rates were configured such that the flame started attached to the burner and then varied until the flame lifted. Finally, flow rates were reduced until the flame reattached to the burner. This process was repeated at various dilution levels.

Figure 4-4 depicts the dependence on initial liftoff velocity on dilution. The jet velocity indicated is the mean flow velocity of the jet at the burner exit. While the undiluted fuels show widely different behavior, it is interesting to note that as dilution increases (decreasing fuel fraction), the dependence on fuel species and burner size decreases. This is evidenced by the convergent nature of the four data sets.

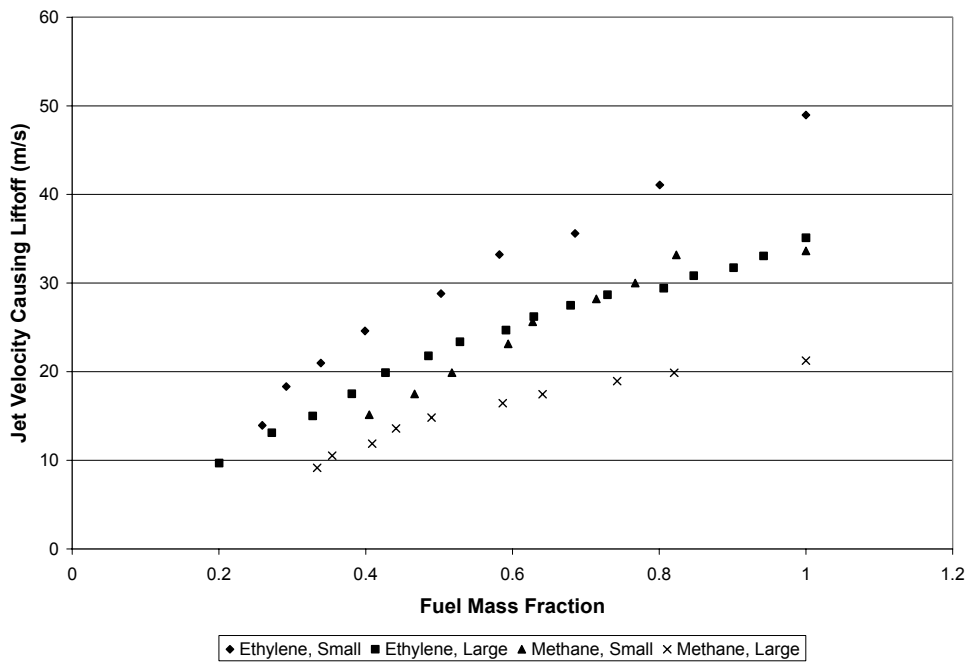


Figure 4-4: Initial Jet Velocity Causing Liftoff for various dilutions

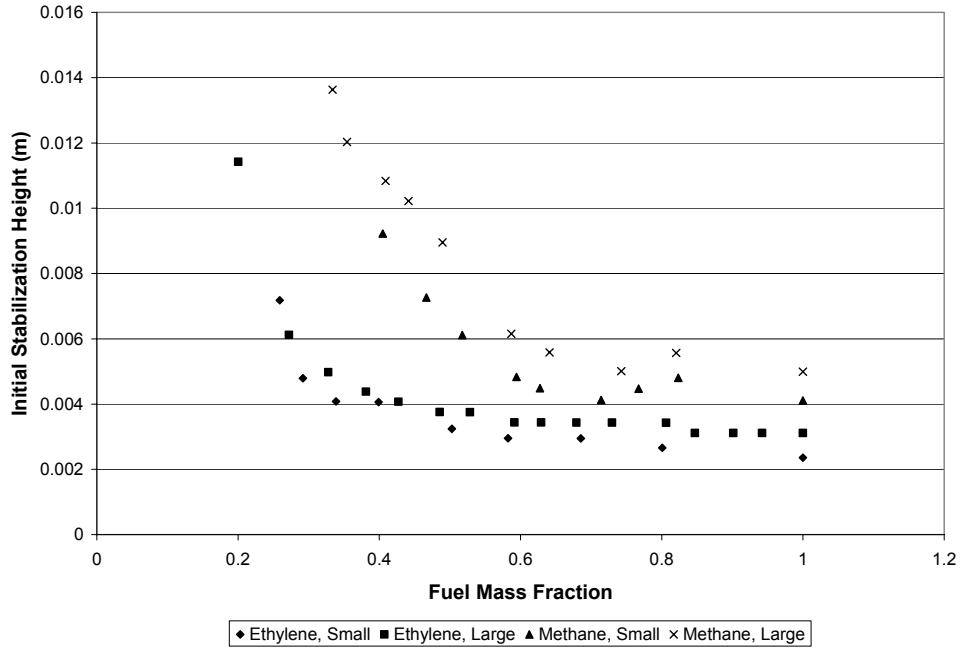


Figure 4-5: Initial Liftoff Height for various dilutions

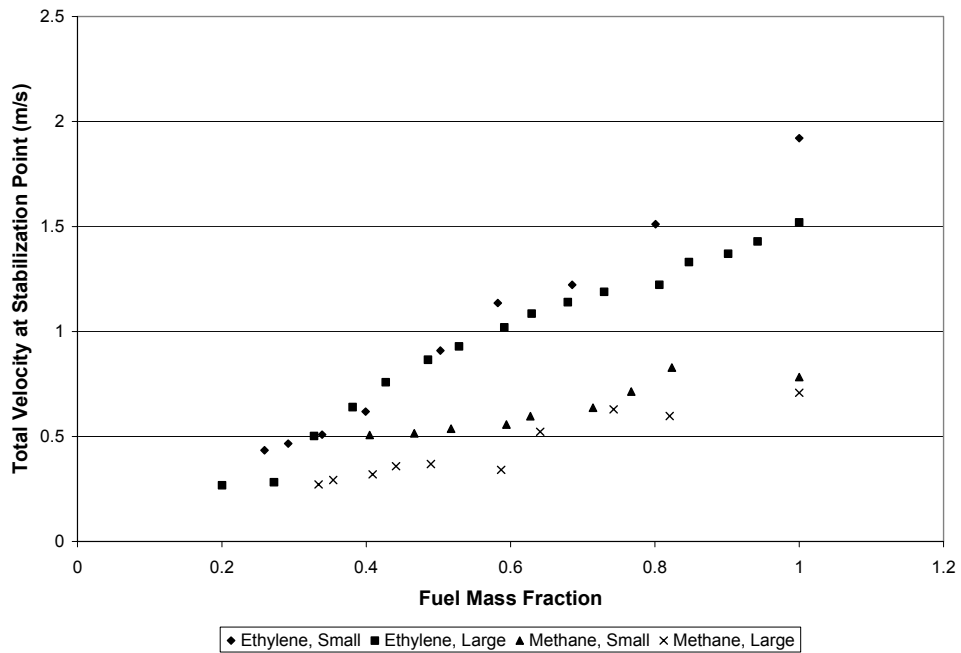


Figure 4-6: Total Velocity at Stabilization Point for various dilutions

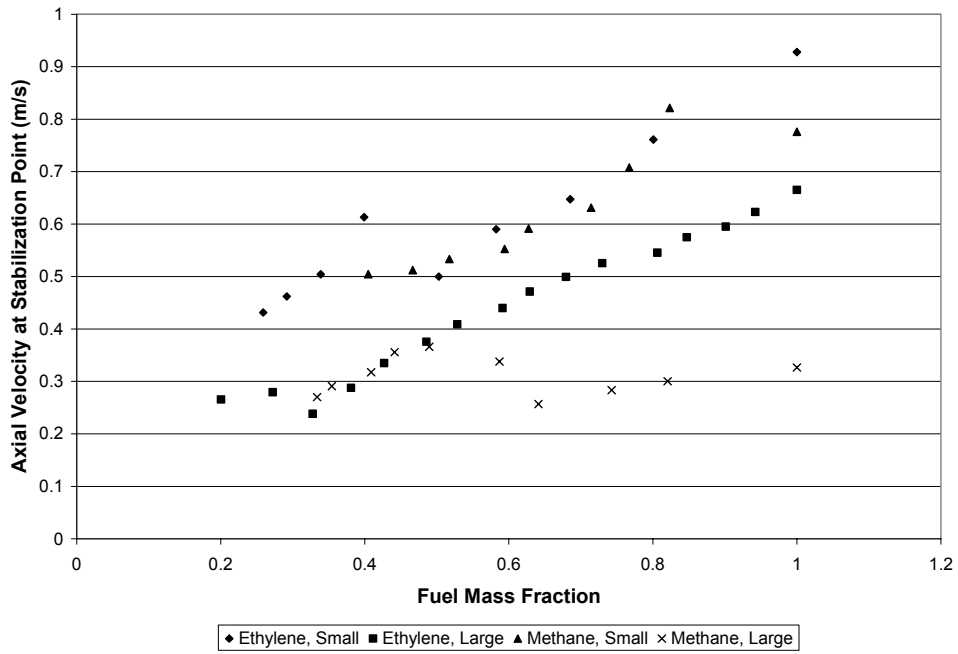


Figure 4-7: Axial Velocity at Stabilization Point for various dilutions

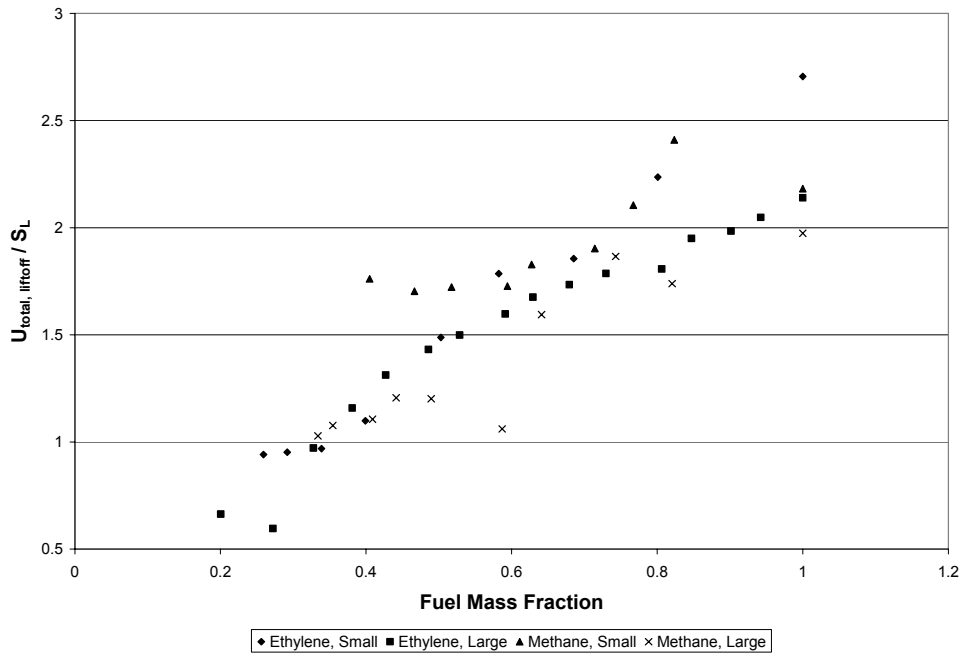


Figure 4-8: Nondimensional liftoff velocity for various dilutions

Figure 4-5 shows the initial liftoff height behavior for ethylene and methane flames at various dilution levels. For both ethylene and methane, the initial lift height behavior exhibits two distinct behaviors. Methane, for example, exhibits an almost constant initial lift height for initial fuel mass fractions greater than 50 percent. For more dilute mixtures, the initial lift height begins to increase dramatically. Ethylene exhibits much the same behavior, only that the transition point is at an initial fuel mass fraction of about 40 percent.

The data presented in Figure 4-6 represents the dependence of the flow field velocity at the initial lifted stabilization point on dilution. While the initial liftoff velocity varied greatly from burner to burner (Figure 4-4), the local flow field velocity is similar from burner to burner (for the same fuel species). The correlation is especially good for fuel fractions less than 0.75. However, the trends exhibit the same convergent behavior as did the initial jet velocity trends (Figure 4-4).

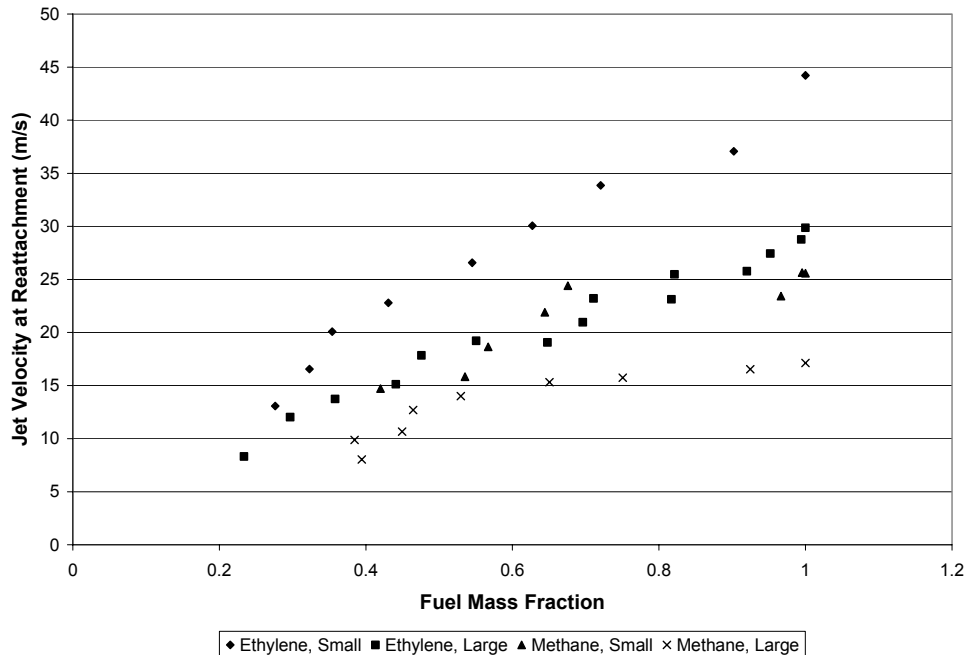


Figure 4-9: Jet Velocity at Attachment for various dilutions

In Figure 4-8, the total stabilization velocity at various dilutions is presented in a nondimensional form. In this case, S_L is the stoichiometric laminar burning velocity for the given fuel/diluent mixture burning in air. With the exception of a few points in the methane data set, the overall data exhibits a linear trend whereby the nondimensional total stabilization velocity increases as fuel mass fraction increases. This data, coupled with the data presented in Figure 4-5, has strong implications for flame stability theory. Based on the idea that the so-called turbulent burning velocity is a function of the laminar burning velocity as well as the turbulence intensity (Gulder [38]), it would appear that dilution decreases a flame's ability to stabilize in regions of high turbulent intensity. This is evidenced by the fact that as dilution increased, the stabilization point velocity approached the laminar burning velocity (stabilization region becoming more laminar).

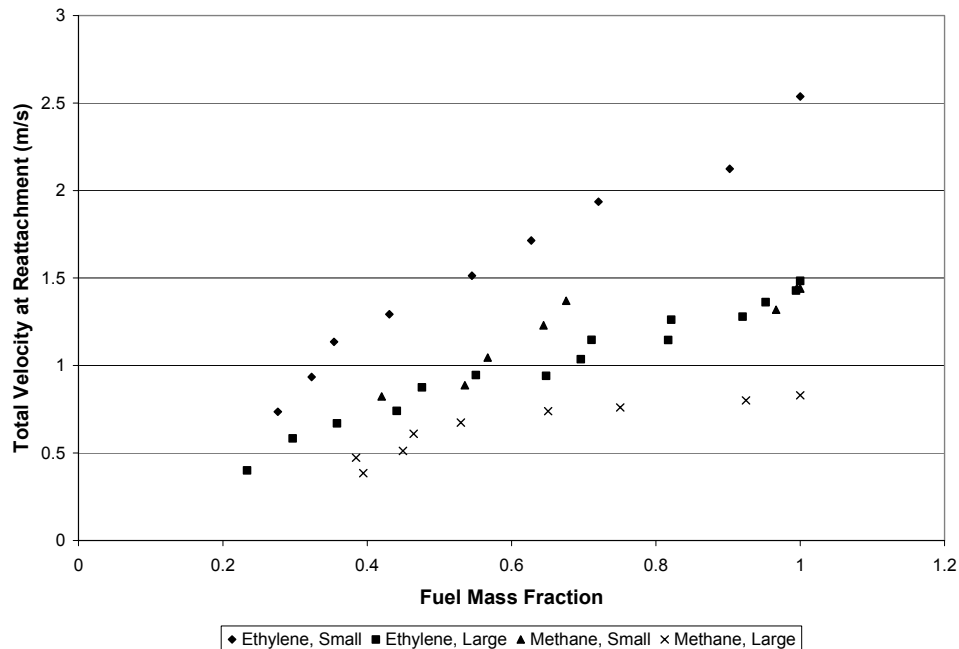


Figure 4-10: Total Velocity at reattachment point for various dilutions

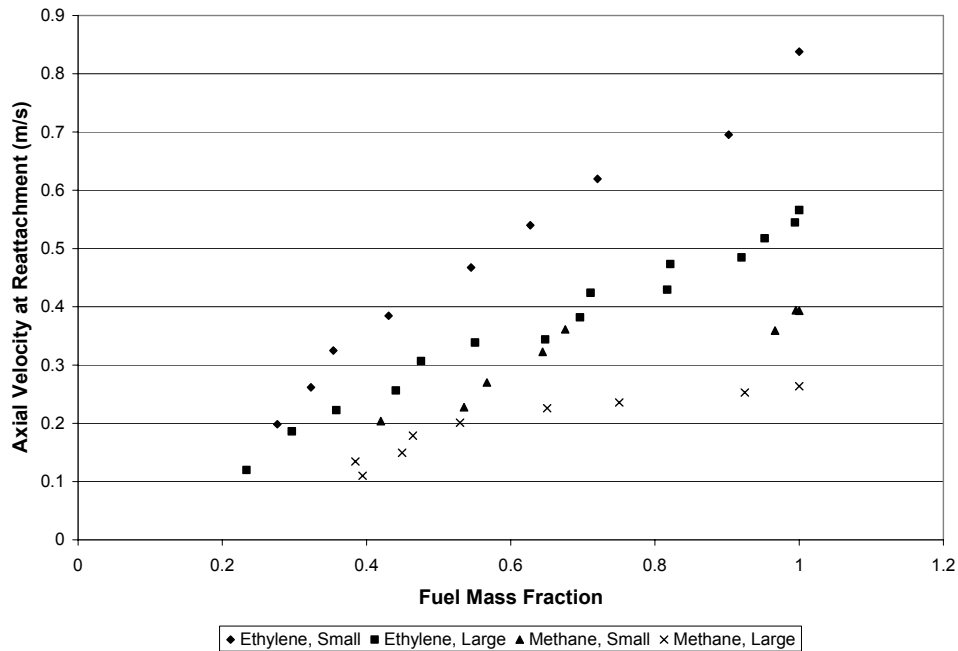


Figure 4-11: Axial velocity at attachment point for various dilutions

Figure 4-9 and Figure 4-10 illustrate the results associated with reattachment of lifted flames. This data set was produced by gradually reducing the flow rates of fuel and diluent until the lifted flame reattached to the burner. Ethylene demonstrates a linear decrease in reattachment jet velocity over the entire range of fuel fractions surveyed. However, methane displays a more-or-less constant reattachment velocity for fuel fractions greater than about 0.4 and a linear decrease in reattachment velocity for fuel fractions less than 0.4.

In general, reattachment data is difficult to pinpoint. This is partially due to hysteresis effects discussed by Terry et al. [4] and Gollahalli et al. [39]. During data collection, it proved to be very easy to overshoot the reattachment point even after a few attempts at the same conditions. In addition, the velocities presented in Figure 4-10, like those in Figure 4-6, are derived from model data. The author tends to question the validity of the velocities predicted by the model extremely close to the jet exit. Questioning stems from

the fact that the total velocity at reattachment is predicted to be higher than the initial liftoff velocity. At the jet exit, the model predicts a perfect top-hat velocity profile. Such a profile is not feasible for a real jet. The assumption of the top-hat profile has little effect on far-field velocity data, but it definitely has an effect on the near-field profiles. Therefore, the data presented in Figure 4-10 should only be viewed in a qualitative fashion. No model will ever accurately predict all aspects of a phenomenon under all circumstances. Indeed the Chu and Lee model was chosen over others (Chen and Rodi [40], Tieszen et al. [9]) due to its ability to give a reasonable model of the physics of the potential core region of an axisymmetric jet. In light of such modeling shortfalls, either actual CFD models (most likely LES or DNS due to reasons previously discussed) or PIV data should be utilized for determining the actual velocity field in the near-field of the jet. Thus, in general, more work needs to be done to develop a better understanding of the reattachment phenomena.

4.1.3 Combined Effects of Co-flow and Dilution

The next study considered involved investigating the combined effects of co-flow and dilution on flame stability. Ethylene was the only fuel considered in this study; nitrogen, again, was the diluent of choice. For four different co-flow velocities (stagnant to 1.05 m/s), the fuel and diluent flow rates were varied to achieve stabilization point data for a wide range of dilution levels and lift heights.

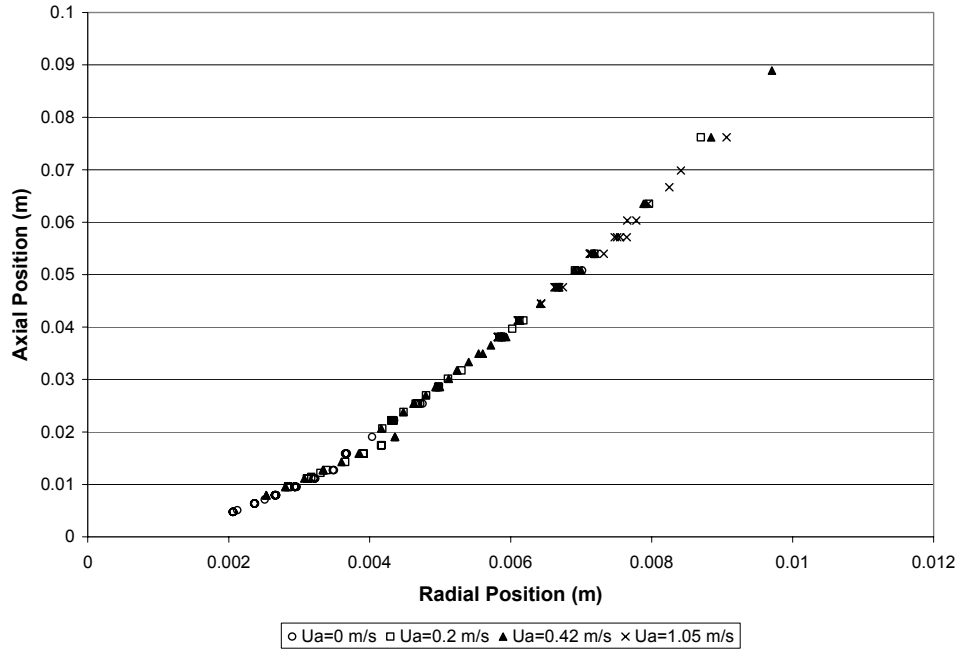


Figure 4-12: Stabilization Point for various initial jet configurations

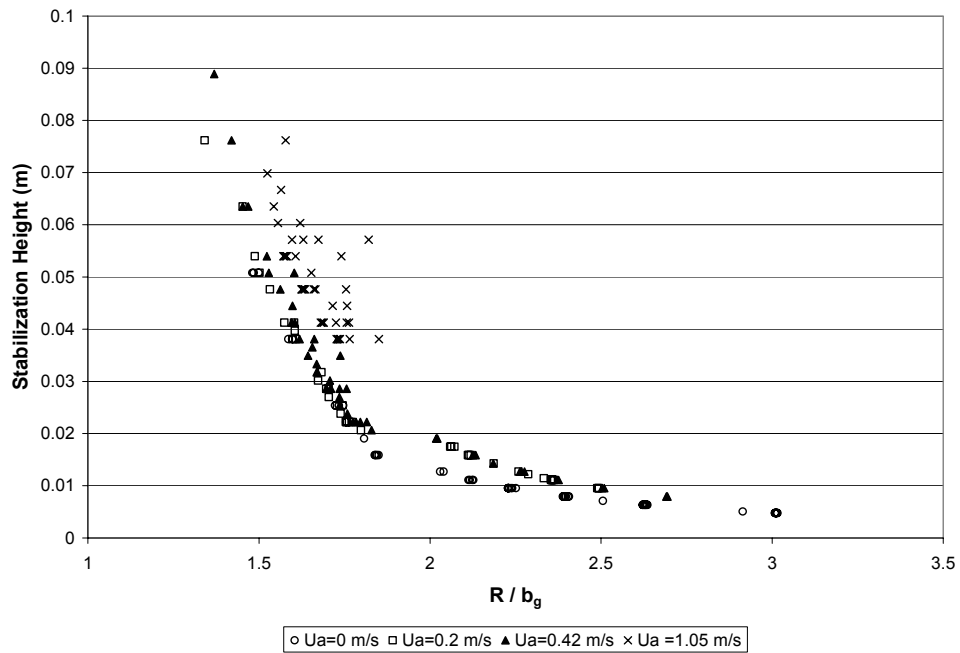


Figure 4-13: Stabilization height and dimensionless radial stabilization location for various jet configurations

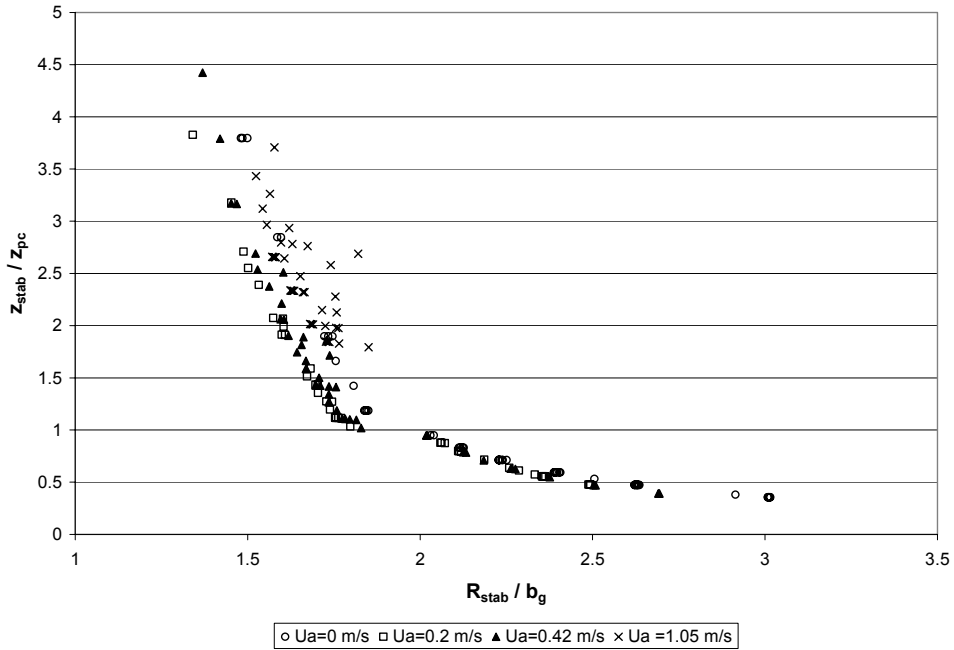


Figure 4-14: Dimensionless Stabilization location for various jet configurations

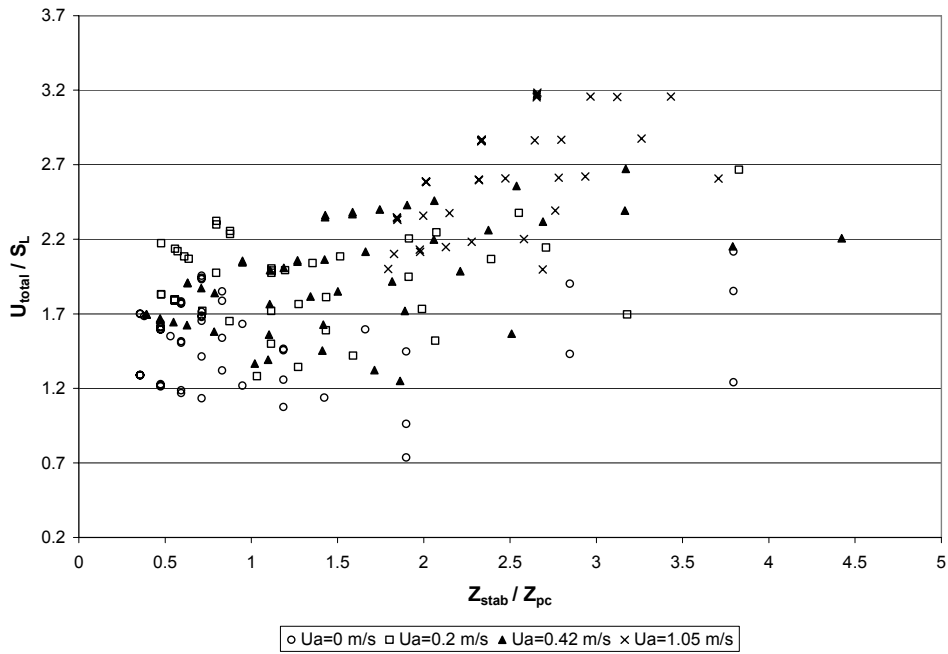


Figure 4-15: Nondimensional stabilization velocity versus nondimensional stabilization height

Figure 4-12 exhibits the stabilization point for all the mixture, initial jet velocity, and co-flow configurations involved in the experiment. While the radial stabilization point was modeled, it is still interesting to note that the axial and radial stabilization position is not greatly affected by dilution or co-flow. This is not to say that co-flow and dilution do not bear on the stability of the flame. Rather, the point is that multiple combinations of co-flow, dilution, and initial jet velocity can have a common stabilization point. Figure 4-13 shows the stabilization height versus a nondimensional radial stabilization position. The term b_g is the radial location where the axial velocity is one-half that at the centerline of the flow field (also known as the jet half-width). This form of nondimensionalization yields information about how different multiple stability points are that share the same global coordinates. It is evident that co-flow and dilution do have a bearing on flame stability. These effects will be discussed further in subsequent sections.

Figure 4-14 introduces another level of refinement to the data presented in Figure 4-13. The difference is that the stabilization height has been nondimensionalized by the length of the potential core of the jet (z_{pc}). This form of nondimensionalization was chosen in an effort to explain the change in profile in Figure 4-13 as evidenced by the discontinuity where R / b_g is approximately 1.8. Figure 4-14 shows that the discontinuity coincides with the end of the potential core region of the jet. Also highlighted is the fact that dilution and/or co-flow have little effect on the relative radial stabilization location of flames stabilizing in the potential core region. The author believes that the gap in the data compiled is because of a sharp discontinuity in the velocity field at the end of the potential core region. Real jets do not exhibit such discontinuities as evidenced by experimental data from Nickels and Perry

[41]. Therefore, questions remain about the region in the immediate vicinity of the discontinuity.

Figure 4-15 denotes the dependence of the stabilization velocity on stabilization height by depicting the trends in the nondimensional quantities. With the exception of a few points, the stabilization velocity is between $1.2S_L$ and $2.5S_L$ for lift heights up to $2Z_{pc}$ (two times the length of the potential core). At higher stabilization positions, the stabilization velocity tends to increase relative to the laminar burning velocity. However, the stabilization velocity does seem to have an upper limit of approximately $3.2S_L$. The increase in stabilization velocity at higher stabilization points is most likely due to increased mixing due to turbulence structures and larger velocity fluctuations.

4.2 Detailed Study of Ethylene Flames

Based on recent publications, much interest now exists in heat-release related theories for non-premixed lifted flame stabilization. One of the main goals of the dilution study was to attempt to ascertain the role of heat-release, if any, in flame stabilization. However, dilution raised another issue: Was the heat release changed by the diluent, or was the flame simply forced to move to a different point in the flow stream to find stoichiometric conditions? Consequently, a more targeted yet still qualitative study was undertaken in an attempt to improve understanding concerning these issues.

4.2.1 Experimental Setup

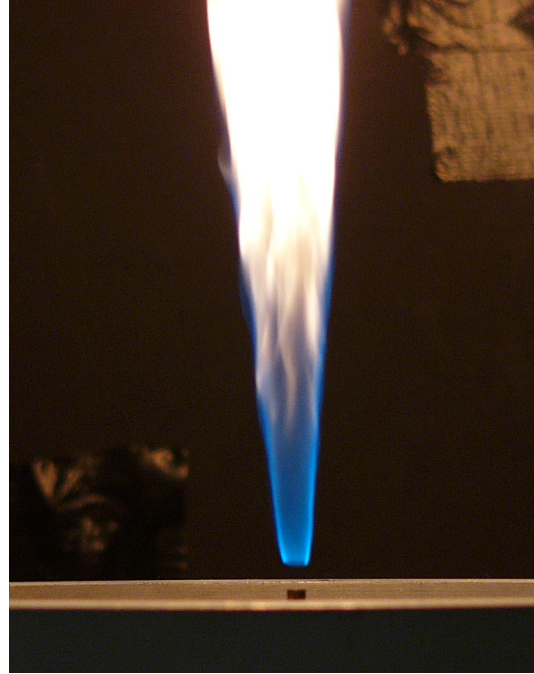
For this portion of the study, much of the equipment remained the same as in the previous study. However, in this study information was needed on the radial size of the flame as well as the stabilization height. To capture this information, the decision was made to photograph the flame and to determine the stabilization point geometry after all data was collected. To image the flame, a four megapixel digital camera was used (Panasonic Lumix DMZ-FC10 with Leica DC Vario-Elmarit 1:2.8/6-72 Aspherical lens). The only shortcoming of this setup is trying to build a temporal-averaged data set. The camera is capable of high shutter speeds (1/2000 second maximum shutter speed). However, the camera is only capable of capturing a few frames per second which is far too infrequent to be able to average the data. So, in an effort to achieve some level of averaging, the shutter speed of the camera was drastically decreased (1/2 second exposure), thereby allowing the camera to “average” the data. Figure 4-16 illustrates the averaging capabilities of this camera. While not ideal, the method did provide reasonably averaged data which was sufficient for drawing qualitative conclusions. The only change to the burner was a switch from a 2.5 mm burner tube to a 3.5 mm burner tube.

4.2.2 Results

Figure 4-17 through Figure 4-24 represents the camera-averaged images of lifted ethylene flames at various levels of dilution and co-flow velocity. Table 4-1 lists the specifics for each image (jet velocity, co-flow velocity, lift height, fuel fraction, and stabilization height). A survey of the images yields two basic conclusions:



(1.0 ms exposure)



(250 ms exposure)

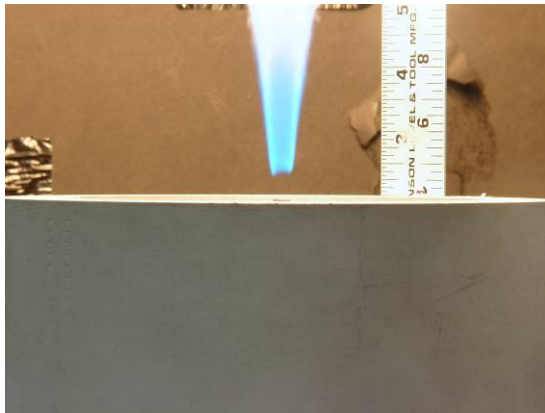
Figure 4-16: Camera-averaged image of methane flame

- The radial stabilization distance does not appear to change significantly from case to case (from dilution and/or from increasing co-flow velocity)
- The flame cone does appear to collapse inward significantly as the dilution level increases

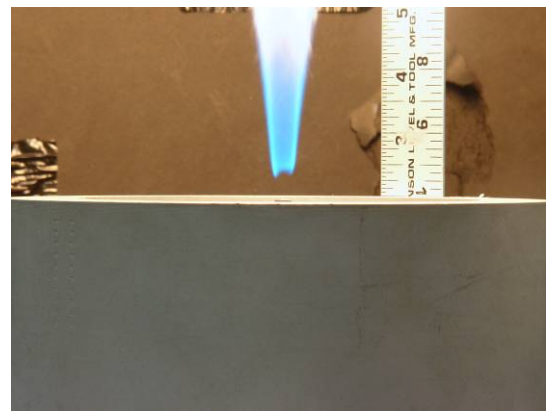
Figure 4-25 and Figure 4-26 depict the radial and axial stabilization data from the study. Modeled radial stabilization data is used in the analysis. Accuracy of modeled results was confirmed with measurements made of select images from Figure 4-17 through Figure 4-24. The points shown in Figure 4-25 are the first and last data points in each set (representing no dilution and high dilution conditions). Figure 4-26 contains all the data points from each set. (Note: the asterisk * denotes model-predicted quantity.)

Table 4-1: Flow Parameters for Images

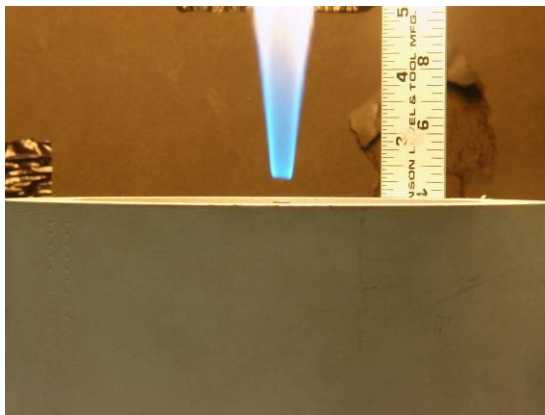
Figure	Image	U_0	U_a	Z_{stab}	$Y_{f,0}$	R_{stab}^*	$U_{stab,ax}^*$	U_{stab}^*
		m/s	m/s	mm		mm	m/s	m/s
Figure 4-17	a	31.1	0	9.525	1.000	3.73	0.59	1.25
	b	26.8	0	9.525	0.883	3.73	0.50	1.08
	c	22.6	0	9.525	0.748	3.74	0.42	0.91
	d	19.3	0	9.525	0.661	3.74	0.35	0.77
	e	17.3	0	9.525	0.512	3.75	0.30	0.69
	f	14.4	0	9.525	0.487	3.76	0.25	0.57
Figure 4-18	a	40.9	0	25.4	1.000	5.93	1.09	1.10
	b	41.2	0	25.4	0.885	5.94	1.09	1.10
	c	37.0	0	25.4	0.781	5.95	0.96	0.97
	d	33.3	0	25.4	0.713	5.96	0.86	0.87
	e	27.4	0	25.4	0.618	5.98	0.69	0.70
	f	23.4	0	25.4	0.553	5.99	0.58	0.59
Figure 4-19	a	22.3	0.33	9.525	1.000	3.58	0.75	1.25
	b	12.8	0.33	9.525	0.840	3.55	0.56	0.79
	c	11.1	0.33	9.525	0.801	3.54	0.53	0.71
	d	9.4	0.33	9.525	0.732	3.53	0.50	0.63
Figure 4-20	a	34.8	0.33	25.4	1.000	6.29	0.98	1.64
	b	31.0	0.33	25.4	0.924	6.29	0.91	1.47
	c	22.5	0.33	25.4	0.732	6.28	0.74	1.11
	d	19.4	0.33	25.4	0.636	6.27	0.67	0.98
	e	15.9	0.33	25.4	0.557	6.25	0.61	0.83
	f	13.9	0.33	25.4	0.505	6.24	0.57	0.75
Figure 4-21	a	26.1	0.67	25.4	1.000	6.16	1.15	1.47
	b	23.6	0.67	25.4	0.906	6.15	1.10	1.37
	c	20.4	0.67	25.4	0.831	6.12	1.04	1.25
	d	17.0	0.67	25.4	0.751	6.07	0.97	1.12
	e	14.2	0.67	25.4	0.623	6.03	0.91	1.02
Figure 4-22	a	35.4	0.67	38.1	1.000	7.25	1.59	1.59
	b	31.2	0.67	38.1	0.900	7.26	1.46	1.46
	c	26.6	0.67	38.1	0.804	7.27	1.31	1.31
	d	23.6	0.67	38.1	0.716	7.27	1.22	1.22
	e	20.0	0.67	38.1	0.638	7.28	1.11	1.11
	f	15.9	0.67	38.1	0.557	7.29	0.99	0.99
Figure 4-23	a	30.1	1.05	38.1	1.000	7.23	1.74	1.74
	b	26.2	1.05	38.1	0.904	7.23	1.62	1.62
	c	21.2	1.05	38.1	0.800	7.23	1.47	1.47
	d	15.8	1.05	38.1	0.659	7.23	1.32	1.32
	e	14.2	1.05	38.1	0.623	7.22	1.27	1.27
Figure 4-24	a	34.8	1.05	50.8	1.000	8.47	1.91	1.92
	b	34.5	1.05	50.8	0.918	8.49	1.90	1.90
	c	30.2	1.05	50.8	0.865	8.50	1.76	1.76
	d	24.7	1.05	50.8	0.756	8.50	1.58	1.58
	e	19.0	1.05	50.8	0.629	8.53	1.40	1.40
	f	15.2	1.05	50.8	0.582	8.53	1.29	1.29



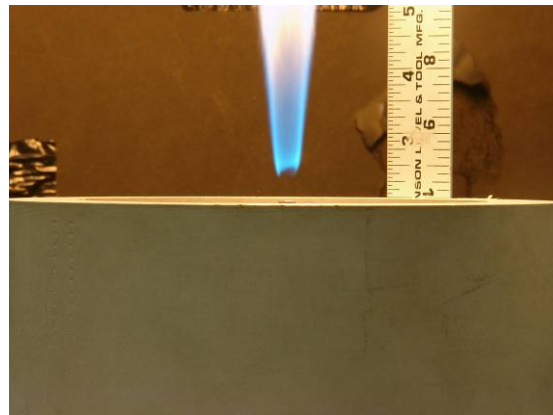
(a)



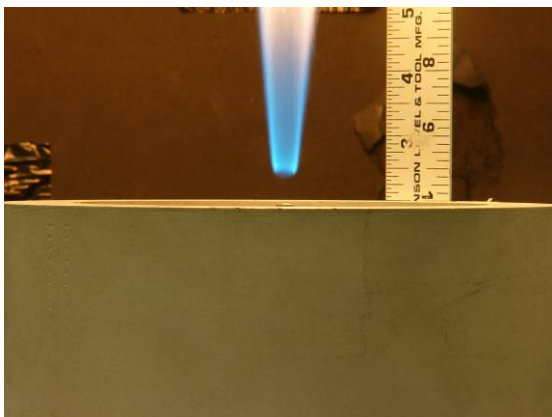
(b)



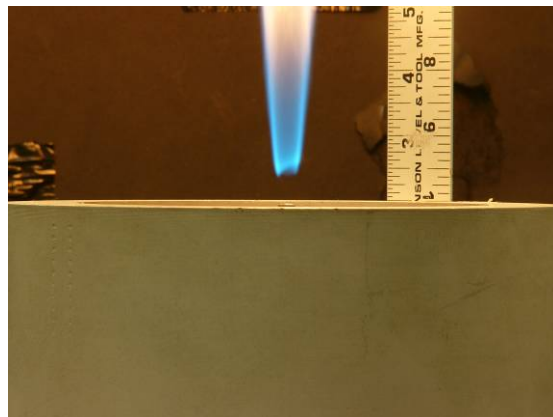
(c)



(d)

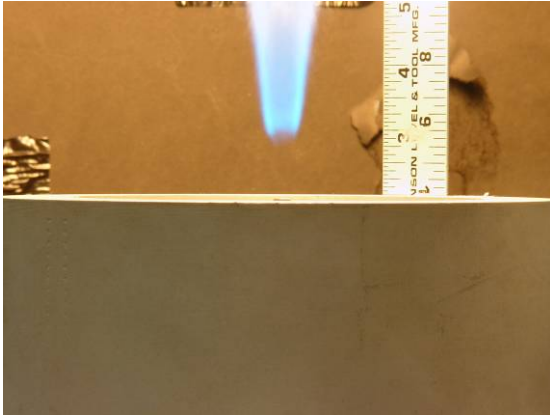


(e)

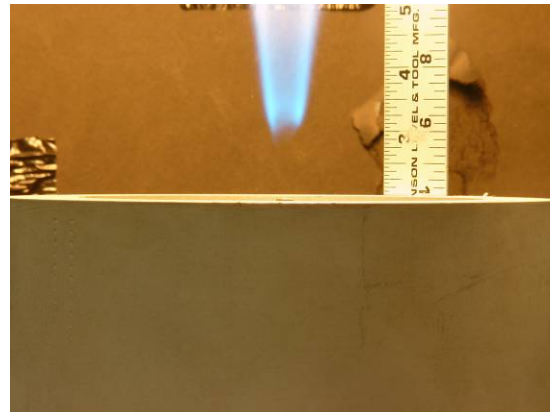


(f)

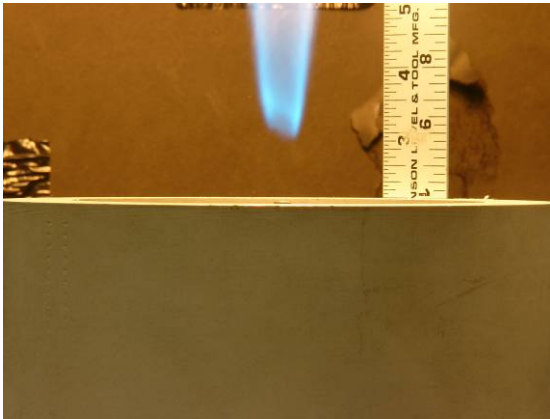
Figure 4-17: Ethylene Flame (low lift height) at increasing dilution levels ($U_a = 0$ m/s)



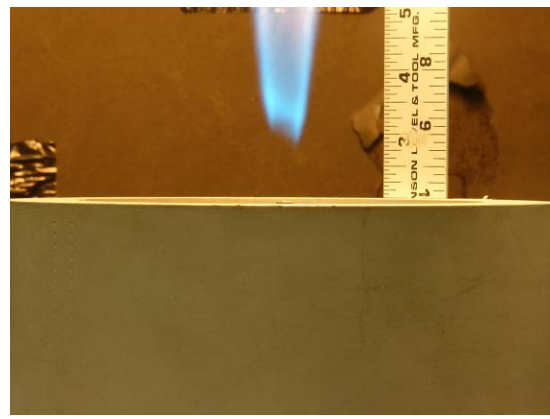
(a)



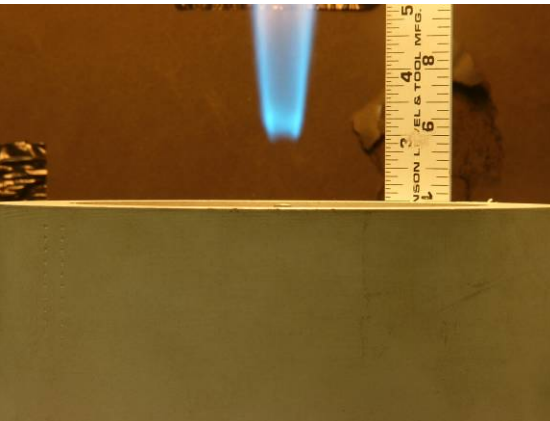
(b)



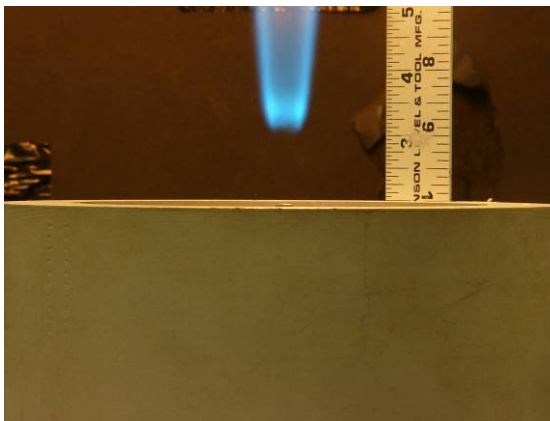
(c)



(d)

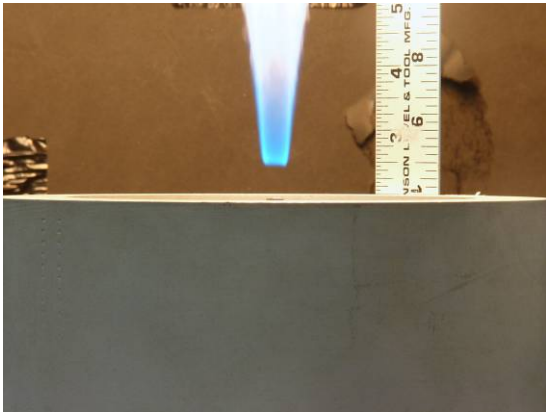


(e)

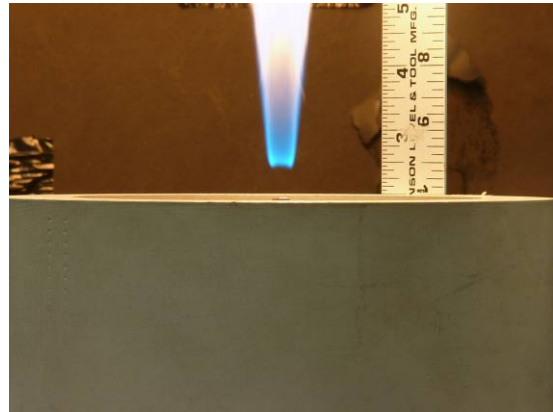


(f)

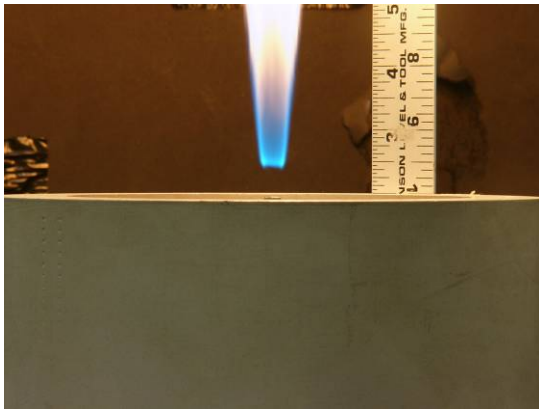
Figure 4-18: Ethylene Flame (high lift height) at increasing dilution levels ($U_a = 0$ m/s)



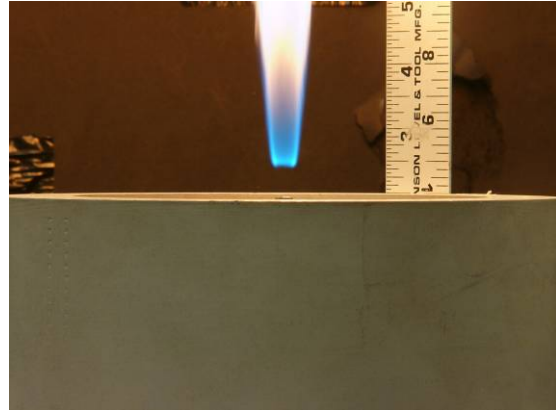
(a)



(b)

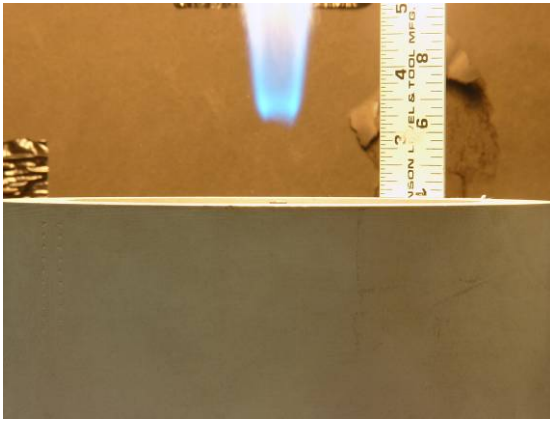


(c)

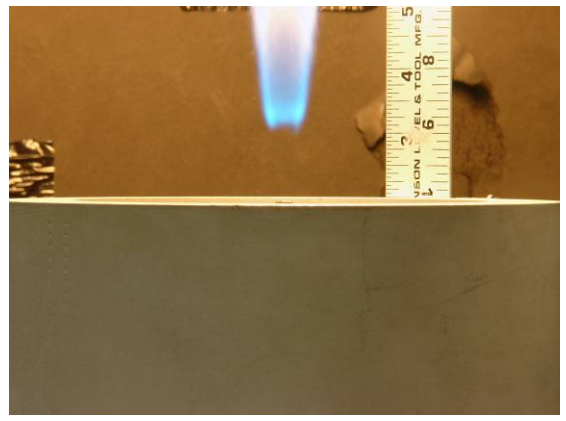


(d)

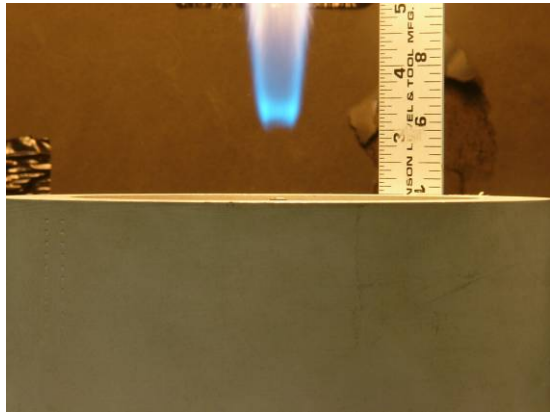
Figure 4-19: Ethylene Flame (low lift height) at increasing dilution levels ($U_a = 0.33$ m/s)



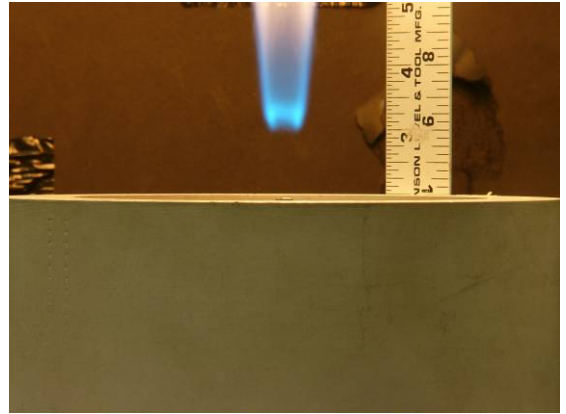
(a)



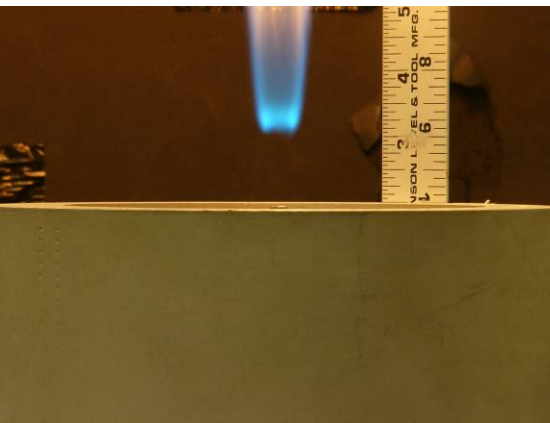
(b)



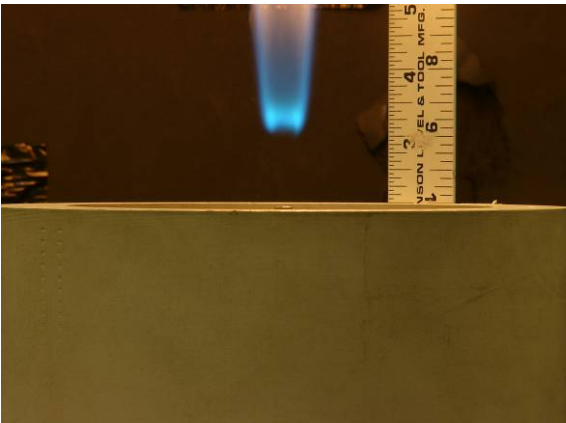
(c)



(d)

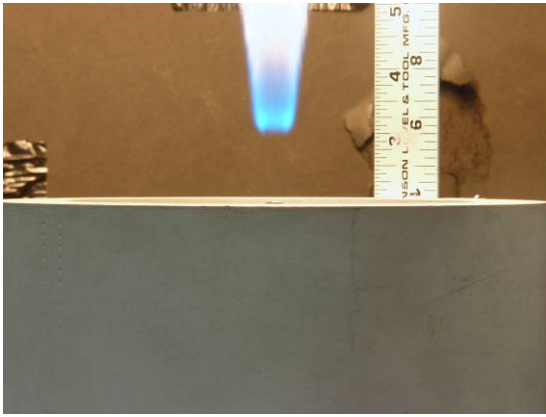


(e)

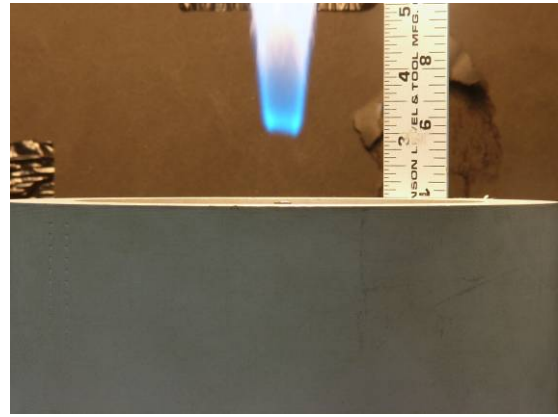


(f)

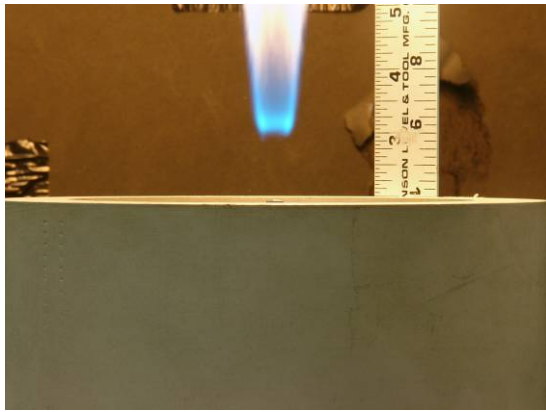
Figure 4-20: Ethylene Flame (high lift height) at increasing dilution levels ($U_a = 0.33$ m/s)



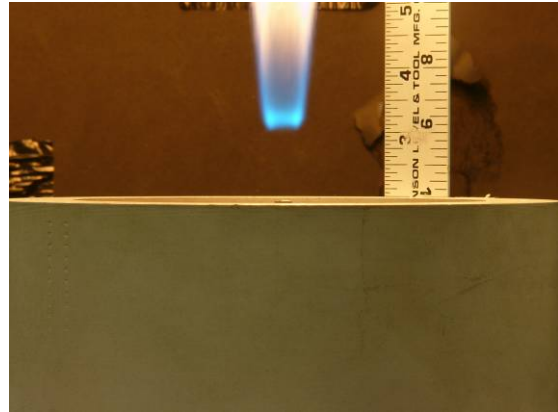
(a)



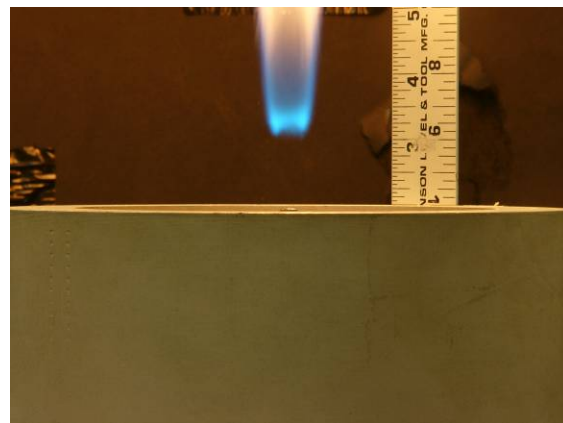
(b)



(c)

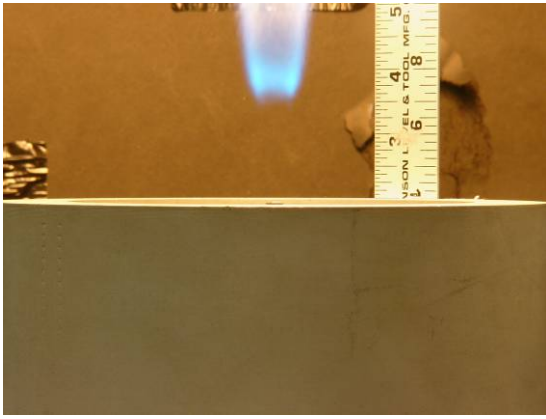


(d)

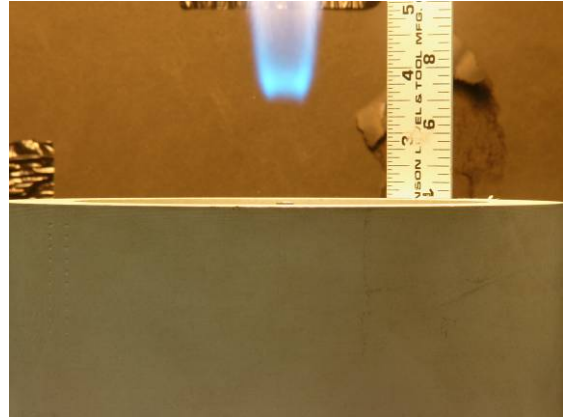


(e)

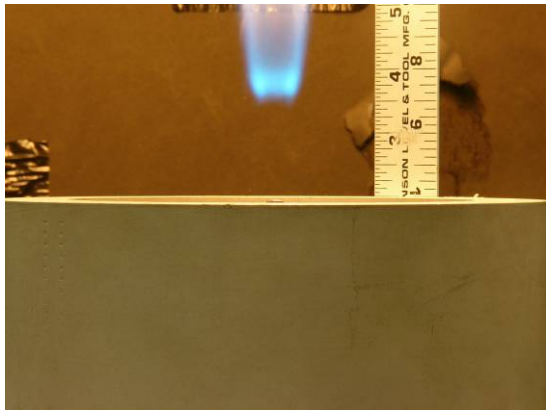
Figure 4-21: Ethylene Flame (low lift height) at increasing dilution levels ($U_a = 0.67$ m/s)



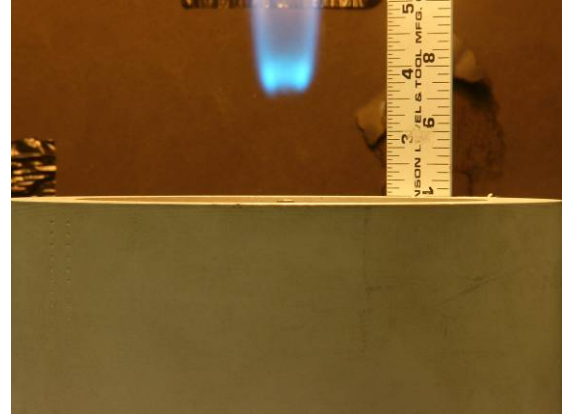
(a)



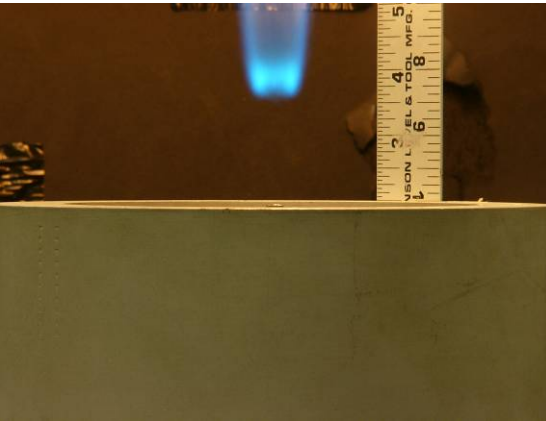
(b)



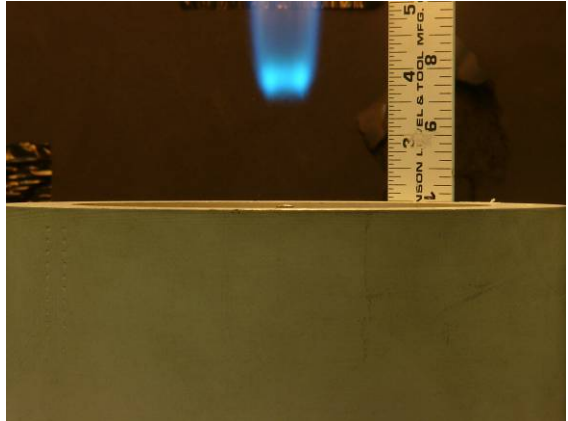
(c)



(d)

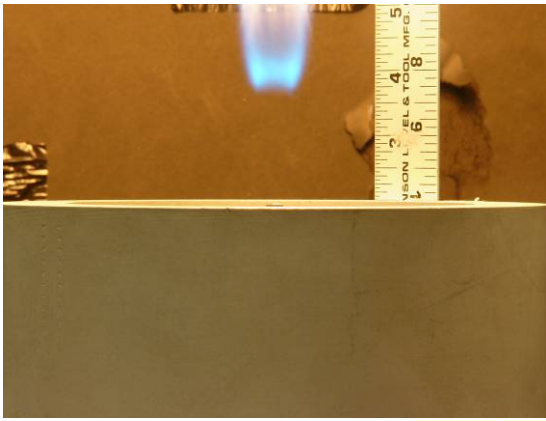


(e)

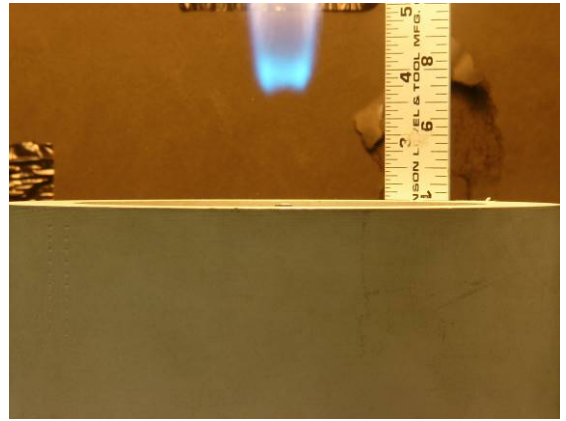


(f)

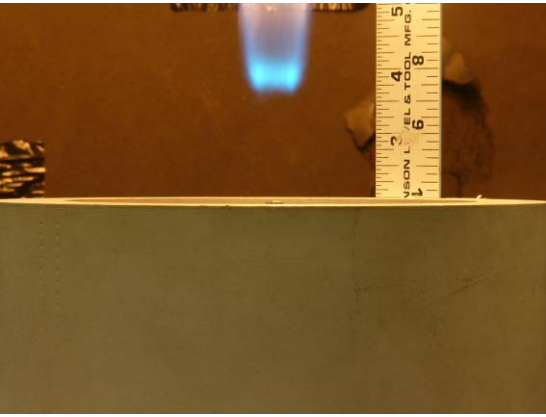
Figure 4-22: Ethylene Flame (high lift height) at increasing dilution levels ($U_a = 0.67$ m/s)



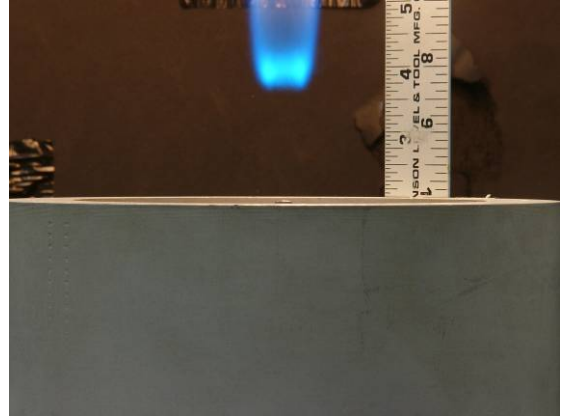
(a)



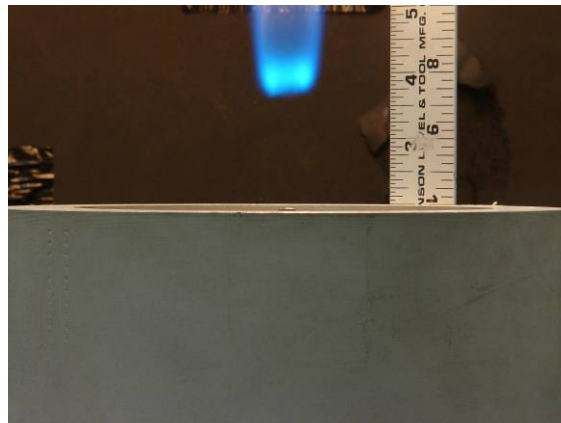
(b)



(c)

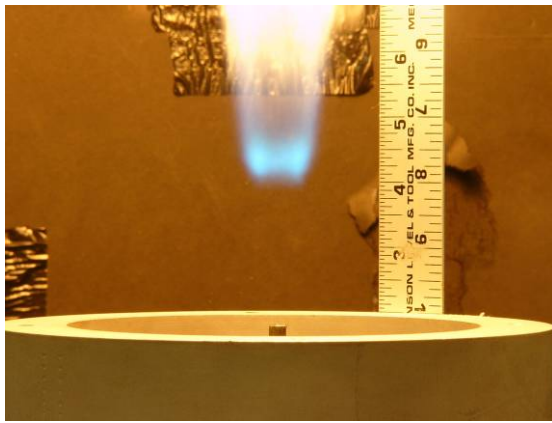


(d)

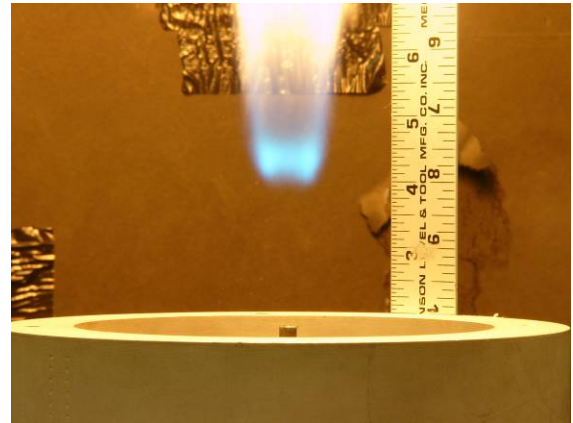


(e)

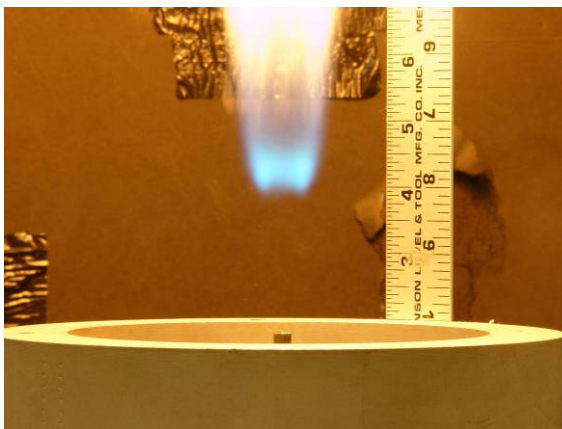
Figure 4-23: Ethylene Flame (low lift height) at increasing dilution levels ($U_a = 1.05$ m/s)



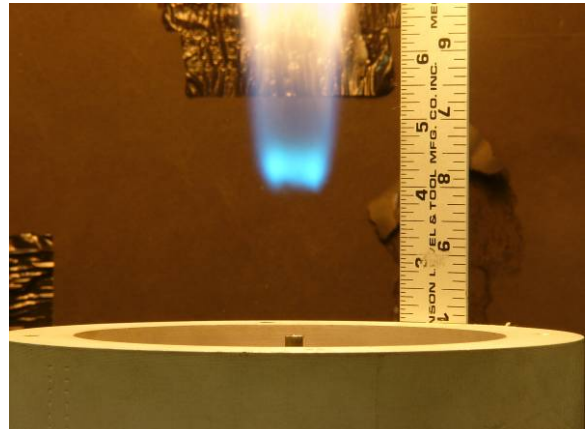
(a)



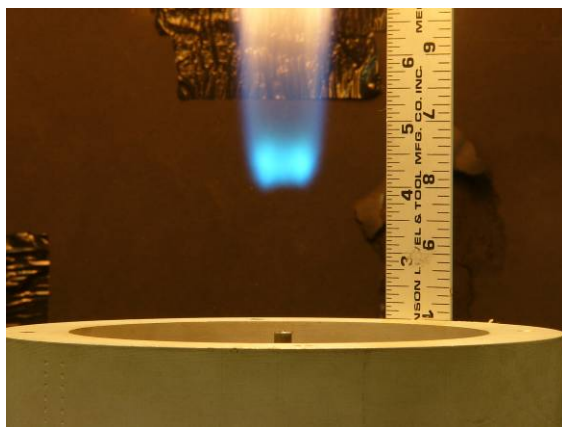
(b)



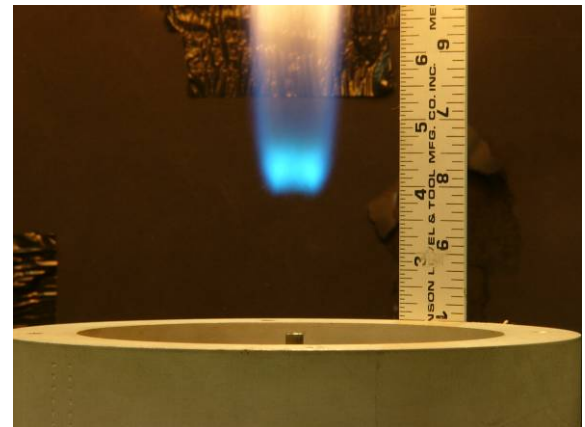
(c)



(d)



(e)



(f)

Figure 4-24: Ethylene Flame (high lift height) at increasing dilution levels ($U_a = 1.05$ m/s)

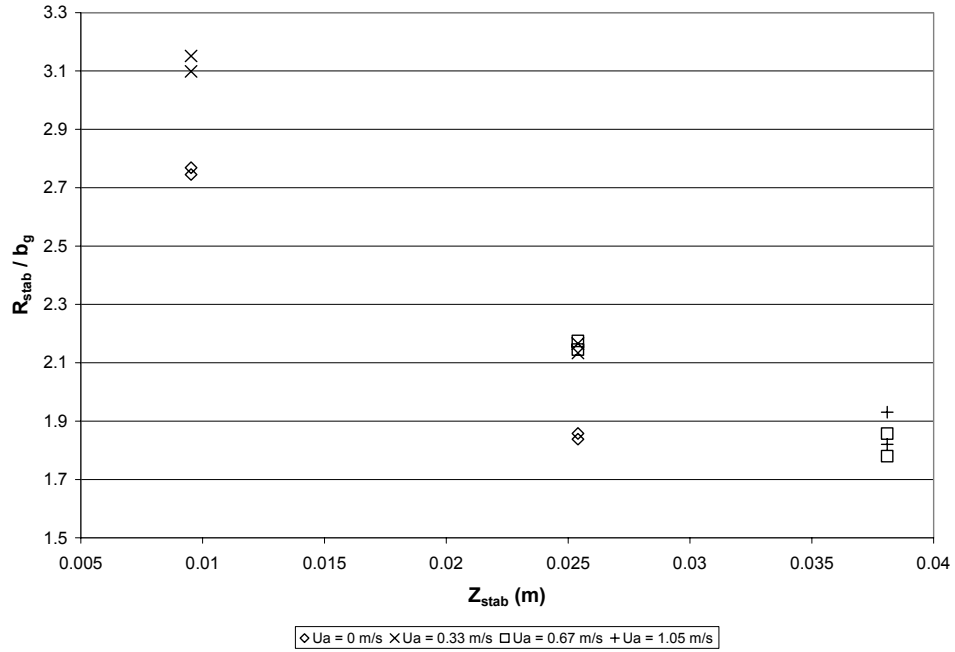


Figure 4-25: Dimensionless Radial Stabilization versus Axial Stabilization

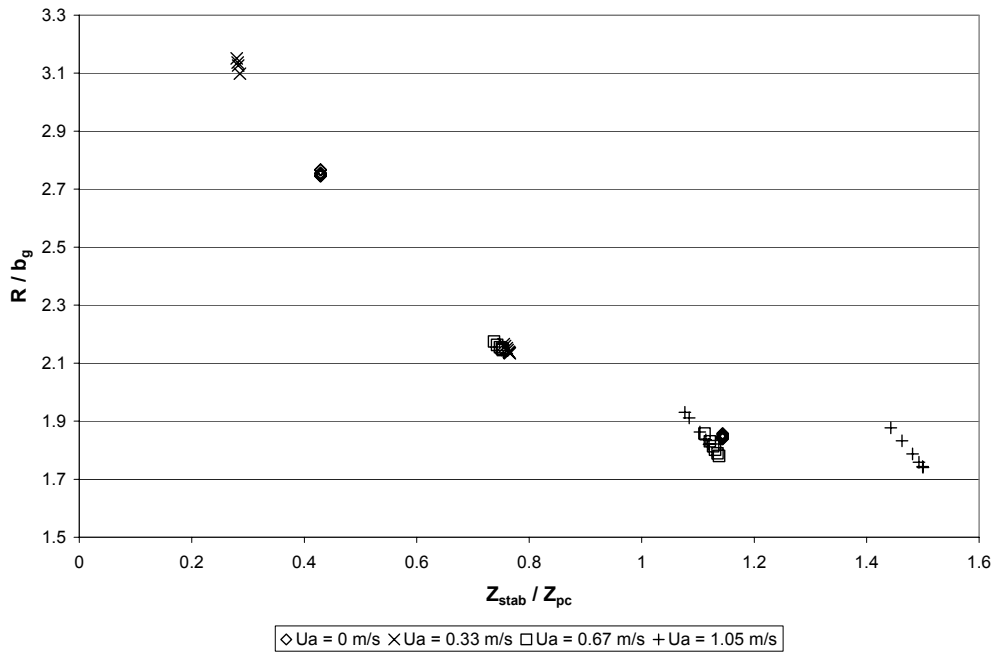


Figure 4-26: Dimensionless Radial Stabilization versus Dimensionless Axial Stabilization

The data presented in Figure 4-25 indicates that, for a given stabilization height, dilution has little effect on the radial stabilization position. However, it would appear that the addition of co-flow shifts the radial stabilization point outward. Figure 4-26 tends to refute this observation. In Figure 4-26, the axial stabilization point is nondimensionalized by the potential core length. This shows that all the flame stability conditions measured fall in a more-or-less linear trend in the potential core region and at a more-or-less constant nondimensional radial distance beyond the potential core. This is due to the effect of co-flow on the potential core (see Figure 4-27).

These results do depend largely on modeled quantities. Confirmation (either experimental or from CFD) of potential core length and jet velocity half width values is needed to confirm these results.

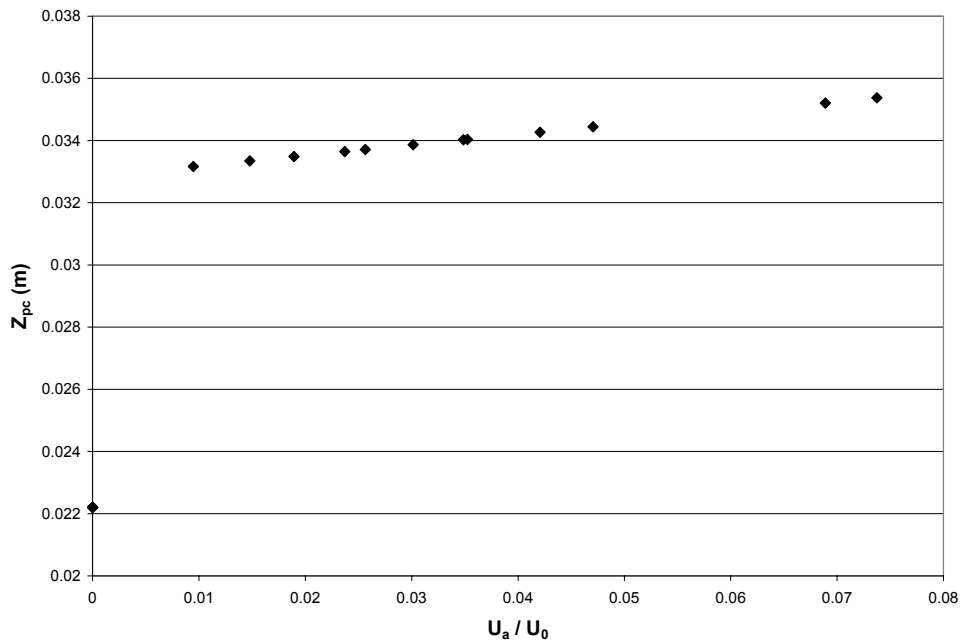


Figure 4-27: Potential Core Length versus Jet Velocity Ratio

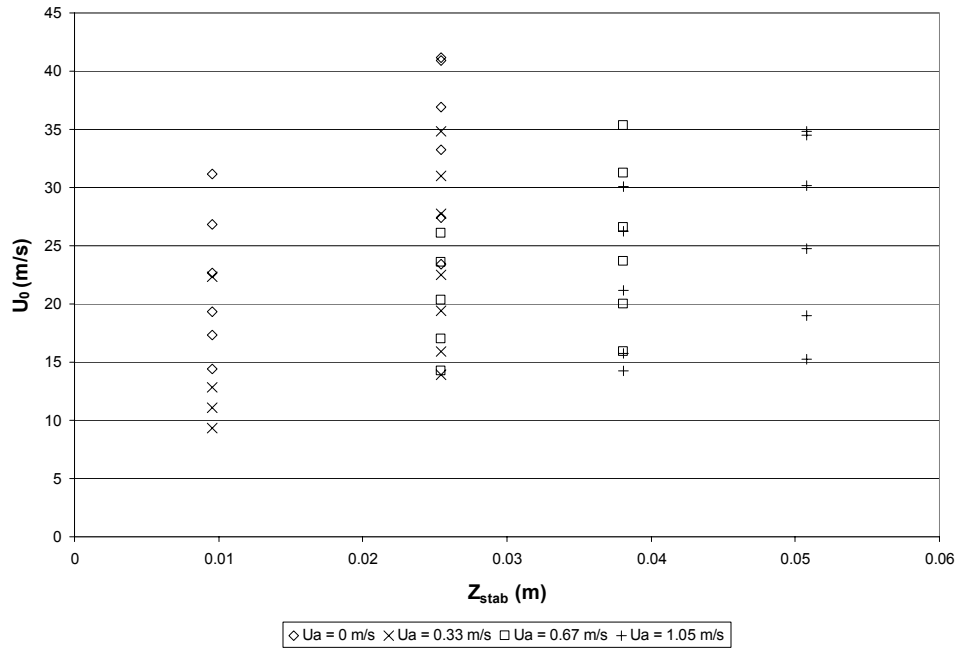


Figure 4-28: Initial Jet Velocity for various lift heights, co-flows, and dilutions

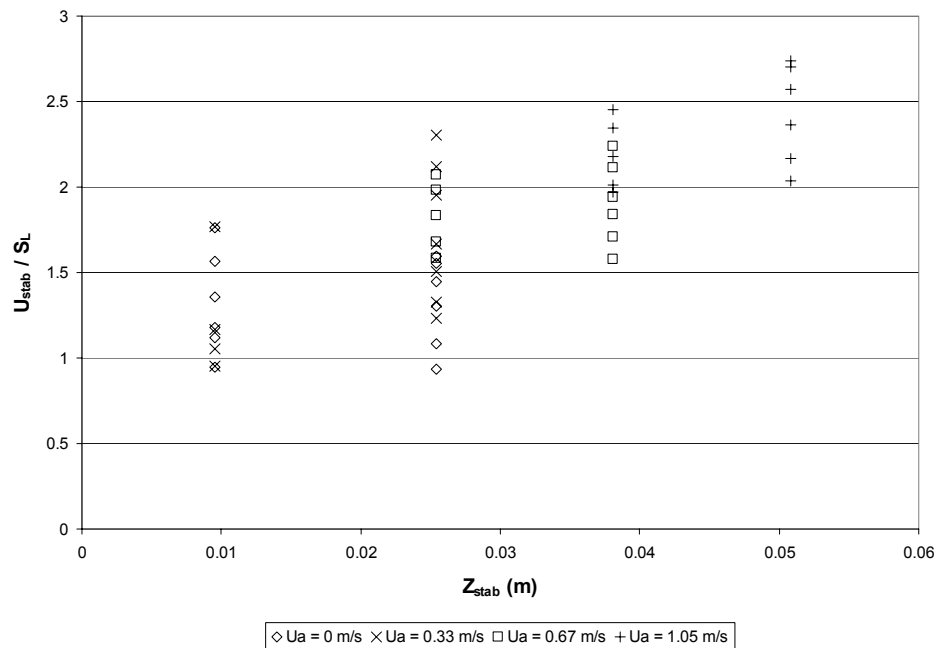


Figure 4-29: Nondimensional stabilization velocity versus lift height

Figure 4-28 illustrates the initial jet velocity needed to stabilize a flame at a given height with a given dilution level and co-flow velocity. For each stabilization height and co-flow condition, the point with the highest jet velocity represents the pure fuel case; the point with the lowest initial jet velocity represents the maximum dilution level tested (refer to Table 4-1 for specific dilution information). This data leads to one main conclusion—both dilution and co-flow reduce the jet velocity needed to lift a flame to a given height.

Figure 4-29 yields more specific information on the effect of dilution and co-flow on stabilization. Just as in Figure 4-28, for each stabilization height and co-flow condition, the point with the highest jet velocity represents the pure fuel case, and the point with the lowest initial jet velocity represents the maximum dilution level tested. It would appear that co-flow actually increases the stabilization point velocity relative to laminar burning velocity (assuming all other factors are held constant). This is evident in all but the lowest lift height case. The effect of dilution is also interesting. If flame stabilization was simply dependent on laminar burning velocity and flow parameters (fluctuations, structures, etc.) and not heat release, the stabilization point velocity should not vary relative to laminar burning velocity. If this were the case, all the points for a given lift height and co-flow condition would fall on top of each other (stabilization velocity would be a constant with respect to laminar burning velocity). However, this is not the case. Increasing the dilution level reduces the stabilization velocity faster than it decreases the laminar burning velocity. This also indicates that the dilution is impacting the flow conditions more than chemistry, since laminar burning velocity is predominately a function of chemistry.

Evidence of the impact of dilution on the flow field can be seen in the photographs in Figure 4-17 through Figure 4-24. The first photograph in each figure is the pure fuel case,

and the last photograph is the highest dilution case tested. In every set the same trend is evident—as dilution increases the flame cone begins to taper inward with the edges of the visible flame transitioning from a conical shape to more of a cylindrical shape. This data, combined with the knowledge that non-participating species basically absorb heat from the combustion process, would tend to confirm the findings of Qin et al. [25] and Upatnieks et al. [26] concerning heat release and streamline divergence.

5 Summary

This research documents experiments and analysis of turbulent, lifted, non-premixed diffusion flames in co-flow and with dilution. The dilution issue is pertinent to understanding how gaseous biofuels will perform in a variety of industrial and commercial burners because biofuels have high concentrations of inert gasses. These inert gasses lower the heating value of the fuels and may have other impacts on the chemistry of the combustion process.

Ethylene and methane were the fuels of choice, and nitrogen was the diluent of choice. Methane was initially chosen because of applicability to biofuels. However, to better evaluate heat release effects, much of the study was performed with ethylene because of its much higher heating value. The belief was that the higher heating value would allow for more resolution in the final data sets.

5.1 Conclusions

Liftoff and reattachment experiments were performed with a fuel jet issuing into a stagnant oxidizer stream (i.e. no co-flow). Several features of the liftoff and reattachment behavior were noted. For one, trends in initial jet velocity needed to induce liftoff showed a marked dependence on jet diameter as well as differences due to fuel species. Ethylene required a larger initial jet velocity to induce liftoff compared to methane. However, all species and jet diameter data sets display similar behavior with respect to dilution. As initial fuel mass fraction decreases, the initial jet velocity requirements also decrease. The magnitude of decrease from no dilution to extinction due to excessive dilution was similar for

all species and initial jet diameter combinations. This would indicate that the overall effect of dilution on initial liftoff is independent of species and initial jet diameter.

Initial liftoff height and local stabilization velocity trends were also observed. For both fuels, initial lift height was more-or-less constant for mixtures at least 50 percent fuel by mass. However, for higher levels of dilution, liftoff height begins to increase dramatically for both fuels. As far as local stabilization velocity trends, both fuels show a linear decreasing trend in local stabilization velocity as fuel mass fraction decreases. There is a jet diameter dependence initially (especially pronounced for ethylene). This dependence disappears about the same time the initial lift height trend changes from constant to rapid increase. An explanation for the disappearance of the diameter dependence is that the velocity field in the far field has little connection with the initial jet diameter. Jet velocities inducing reattachment displayed similar trends to the corresponding liftoff data. However, data concerning local stabilization velocity is flawed due to a breakdown of the jet model very close to the jet exit. Thus, no conclusions are drawn concerning the flame/flow field interactions at reattachment.

Combined effects of co-flow and dilution were also addressed. For one, it was found that the stabilization point (axial and radial coordinates) all fall on one smooth trend. This may partially be a modeling effect. The radial stabilization point was modeled based on the flame stabilizing at stoichiometric conditions. However, subsequent photographic investigations seem to corroborate this assumption. The trend did expand when the radial stabilization position was nondimensionalized by the velocity half-width of the jet (radial distance where the axial velocity is one-half that of the velocity at the centerline), and the stabilization height was nondimensionalized by the length of the potential core. This

illustrated that stabilization points in the potential core region fall more-or-less on the same profile. This would indicate that the strong shearing effects at work as well as steep velocity and scalar gradients present in the potential core region would tend to negate effects of co-flow or dilution when determining the radial stabilization distance. Beyond the potential core, co-flow effects on radial stabilization position were evident. As stabilization height increases, the radial stabilization point moves closer to the velocity half-width of the jet. However, co-flow tends to move the stabilization point away from the velocity half-width.

As previously noted, stabilization velocity decreased as dilution increased. Targeted studies, where lift height was maintained over a range of dilution levels, and co-flow conditions confirmed this as well as showed that dilution tended to increase the stabilization velocity (relative to either zero co-flow data or data at lower co-flow values). The more profound realization was that as dilution increased stabilization velocity decreased faster than laminar burning velocity. Diluents, like any other non-participating species, tend to simply absorb heat from the combustion process. Thus, increased levels of diluents would decrease the heat available to affect the flow region around the flame. Diluents would also tend to affect the combustion process itself. However, those effects would be captured in the decrease in laminar burning velocity. Stabilization velocity decreasing faster than laminar burning velocity with increasing dilution could still be permissible under turbulent burning velocity theory if the decrease was due to decreasing velocity fluctuations. However, the data collected shows strong stabilization velocity decreases for relatively small changes in flow field velocity. (Note: no velocity fluctuation data was available for this analysis.) Thus, the heat release effects discussed by Ruetsch [23], Boulanger [24], Qin [25], and Upatineks

[26] would tend to be the more plausible mechanism for lifted flame stabilization based on these findings in this study.

Photographic studies seem to support the findings of Qin et al. [25] concerning streamline divergence. In their numerical analysis, they found that heat released tended to raise the pressure inside the flame and that this increased pressure caused the flame front to behave like a solid body in the flow field. This action caused streamlines to diverge upstream of the flame front just as streamlines would diverge around a leading edge of an aircraft wing. The photographic evidence supports this finding but on a larger scale. It was noted in every case that, for a given stabilization height as dilution increased, the flame collapsed inward more and more. With no dilution, the overall flame shape was conical. However, as dilution increased the flame surface moved toward parallel with the flow axis. At maximum tested dilution, the flame was almost cylindrical in every case.

Reduction in heat release coupled with increasing initial lift heights has implication for the theoretical works of Ruetsch et al. [23] and Boulanger et al. [24]. In their works lift height was predicted to increase dramatically when the effects of heat release were removed from the analysis. Dilution is the only physical way to remove heat from the combustion system and maintain all other aspects of combustion. Just as their works predicted, initial lift heights increased dramatically as heat was removed.

5.2 Future Work

Future work that would be appropriate for furthering the findings from this study fall into two categories:

- Flow field measurements to augment modeled quantities
- Expand range of fuels/diluents considered

Direct measurements of flow fields and flame locations would be very useful for confirming or refuting this study's findings. This is because so many quantities were modeled: flow field velocities, radial stabilization location, etc. The jet model used has been proven to under predict flow field velocities, and there are concerns about the region around the end of the potential core. A combination of PIV for velocity and some species fluorescence (either OH fluorescence or CH fluorescence) for flame location would provide experimentally all the quantities that were modeled.

Expanding the scope of fuels and diluents considered would be appropriate to determine if the effects described in this study are unique to the fuels and diluent used or are indicative of larger trends. For example, the fuels that were used all have Schmidt numbers less than one. Expanding the research to fuels with Schmidt numbers greater than one, such as propane, could provide valuable information to determine if the effects seen in this study were biased by a certain mass diffusion behavior. Other diluents could also provide valuable information. The use of totally non-reactive diluents (helium, argon, neon, etc.) could be used to isolate chemistry effects from heat effects, with respect to changes in dilution. Nitrogen can potentially participate in combustion reactions, so it is difficult to ascertain the extent of effects on heat release and on chemistry. Carbon dioxide as a diluent could provide

more data pertinent to the field of biogas, as most biogas is naturally diluted with carbon dioxide, not nitrogen. Also, carbon dioxide has other properties relating to radiation heat transfer that are not as strong in nitrogen. Thus, carbon dioxide could provide more enhanced understanding of the heat release effect.

6 References

1. Chemical Composition of Natural Gas. Union Gas. 1 March 2005
<<http://www.uniongas.com/aboutus/aboutng/composition.asp>>.
2. IEA Bioenergy. Biogas Flares: State of the Art and Market Review. December 2000. Nova Energie. 1 March 2005 <http://www.novaenergie.ch/iea-bioenergy-task37/Dokumente/Flaring_4-4.PDF>.
3. Jensen, J. and Jensen, A. Biogas and Natural Gas Fuel for the Future. 2000. Danish Gas Technology Center. 1 March 2005
<<http://uk.dgc.dk/pdf/Sevilla2000.pdf>>.
4. Terry, S.D. On Flame Stability in the Hysteresis Regime in Co-flow. Raleigh, NC, 2005.
5. Vanquickenborne, L. and Van Tiggelin, A., "The stabilization mechanism of lifted diffusion flames." Combustion and Flame 10 (1966): 59-69.
6. Eickhof, H., Lenze, B., and Leuckel, W., "Experimental Investigation of the Stabilization Mechanism of Jet Diffusion Flames." The Combustion Institute Twentieth Symposium (International) on Combustion (1984): 311-318.
7. Kalghatgi, G., "Lift-off Heights and Visible Lengths of Vertical Turbulent Jet Diffusion Flames in Still Air." Combustion Science & Technology 41 (1984): 17-29.
8. Brown, C.D., Watson, K.A., Lyons, K.M., "Studies on lifted jet flames in co-flow: the stabilization mechanism in the near- and far-fields." Flow, Turbulence and Combustion 62 (1999): 249-273.
9. Tieszen, S., Stamps, D., and O'Hern, T. "A heuristic model of turbulent mixing applied to blowout of turbulent jet diffusion flames." Combustion and Flame 106 (1996): 442-466.
10. Watson, K.A., Lyons, K.M., Donbar, J.M., and Carter, C.D., "Scalar and velocity field measurements in a lifted methane-air diffusion flame", Combustion and Flame 117 (1999): 257-271.
11. Peters, N. and Williams, F.A., "Liftoff characteristics of turbulent jet diffusion flames." American Institute of Aeronautics and Astronautics 21 (1983): 423-429.
12. Broadwell, J.E., Dahm, W.J.A, and Mungal, M.G., "Turbulent Mixing and Combustion in a Reacting Shear-Layer." The Combustion Institute Twentieth Symposium (International) on Combustion (1984):303-310.
13. Miake-Lye, R.C. and Hammer, J.A., The Combustion Institute Twenty-Second Symposium (International) on Combustion (1988): 817-824.
14. Dahm, W.J.A. and Dibble, R.W., The Combustion Institute Twenty-Second Symposium (International) on Combustion (1988): 801-808.

15. Pitts, W.M., "Large scale turbulent structures and the stabilization of lifted turbulent jet diffusion flames." The Combustion Institute Twenty-Third Symposium (International) on Combustion (1990): 661-668.
16. Byggstoyl, S. and Magnussen, B.F., "A model for flame extinction in turbulent flow." Turbulent Shear Flows 4th ed. Ed. Bradbury, L.J.S., Durst, F., Launder, B.F., Schmidt, F.W., and Whitelaw, J.H. Berlin: Springer-Verlag, 1985. 381.
17. Phillips, H. Proceedings of the Combustion Institute 10 (1965): 1277-1283
18. Kioni, P. N., Rogg, B., Bray, K. N. C., and Liñán, A. "Flame Spread in Laminar Mixing Layers—The Triple Flame." Combustion and Flame 95 (1993): 276-290
19. Plessing, T., Terhoeven, P., Peters, N., and Mansour, M. S. "An experimental and numerical study of a laminar triple flame." Combustion and Flame 115 (1998): 335-353.
20. Muñiz, L. and Mungal, M.G., "Instantaneous flame-stabilization velocities in lifted jet diffusion flames." Combustion and Flame 111 (1997): 16-31.
21. Watson, K.A., Lyons, K.M., Donbar, J.M., and Carter, C.D., "Observations on the leading edge in lifted flame stabilization." Combustion and Flame 119 (1999): 199-202.
22. Su, L. K., Han, D., and Mungal, M. G., Proceedings of the Combustion Institute 28 (2000): 327-334.
23. Ruetsch, G. R., Vervisch, L., and Liñán, A. "Effects of heat release on triple flames," Physics of Fluids 7(6) (1995): 1447-1454.
24. Boulanger, J., Vervisch, L., Reveillon, J., Ghosal, S. "Effects of heat release in laminar diffusion flames lifted on round jets," Combustion and Flame 134 (2003): 355-368.
25. Qin, X., Choi, C. W., Mukhopadhyay, A., Puri, I. K., Aggarwal, S. K., and Katta, V. "Triple flame propagation and stabilization in a laminar axisymmetric jet," Combustion Theory and Modeling 8 (2004): 293-313.
26. Upatnieks, A., Driscoll, J. F., Rasmussen, C. C., and Ceccio, S. L. "Liftoff of turbulent jet flames – assessment of edge flame and other concepts using cinema-PIV," Combustion and Flame 138 (2004): 259-272.
27. Glassman, I. Combustion, San Diego. Academic Press, 1996.
28. Kuo, K. Principles of Combustion, New York. John Wiley & Sons, 1986.
29. T. Echekki and M. G. Mungal, "Particle Tracking in a Laminar Premixed Flame," Physics of Fluids A, 2(9) (1990): 1523.
30. Clingman, W.H. Jr., Brokaw, R.S., and Pease, R.D. Int. Symp. Combust., 4th (1953) p. 310. In Glassman, I., Combustion, Academic Press, New York (1977) p. 85.
31. Cho, J. R. and Chung, M. K. "A k-epsilon-gamma [$k-\epsilon-\gamma$] equation turbulence model," Journal of Fluid Mechanics 237 (1992): 301-322.

32. Merci, B. and Dick, E. "Predictive Capabilities of an Improved Cubic k-epsilon [$k-\epsilon$] Model for Inert Steady Flows," Flow, Turbulence and Combustion 68 (2002): 335-358.
33. Jaw, S. W. and Chen, C. J. "Present Status of Second Order Closure Turbulence Models; II. Applications," Journal of Engineering Mechanics (1998): 502-512.
34. Chu, V. and Lee, J. Turbulent Jets and Plumes: A Lagrangian Approach, Boston. Kluwer Academic Publishers, 2003.
35. Mathews, J. H., Fink, K. D. Numerical Methods Using Matlab, 4th ed, Prentice-Hall. Upper Saddle River, NJ, 2004
36. Weisstein, E. W. "Lagrange Interpolating Polynomial," Mathworld – Wolfram <<http://mathworld.wolfram.com/LagrangeInterpolatingPolynomial.html>>
37. Watson, K. Experimental Studies on the Leading Edge and Local Extinction in Lifted-Jet Diffusion Flames. Raleigh, NC 2005.
38. Gulder, O.L., "Turbulent premixed flame propagation models for different combustion regimes." The Combustion Institute Twenty-third symposium (international) on combustion (1990): 743-750.
39. Gollahalli, S. R., Savaş, Ö., Huang, R. F., and Rodriguez Azara, J. L. "Structure of attached and lifted gas jet flames in hysteresis region." The Combustion Institute Twenty-first Symposium (International) on Combustion (1986): 1463-1471.
40. Chen, C. and Rodi, W. Vertical Turbulent Buoyant Jets – A Review of Experimental Data. New York. Pergamon Press, 1980.
41. Nickels, T.B. and Perry, A.E. "An experimental and theoretical study of the turbulent co-flowing jet," J. Fluid Mech., 309 (1996) 157-182.
42. Linnett, J. W. and Hoare, M. F. "Burning Velocity Determination: Part III – Burning Velocities of Ethylene + Air + Carbon Dioxide Mixtures", Transactions of the Faraday Society. 47 (2): 179-183 1951.
43. Peters, N. and Rogg, B. Reduced Kinetic Mechanisms for Applications in Combustion Systems, New York. Springer-Verlag, 1993.

7 Appendix

7.1 Appendix I: CHEMKIN Reaction Mechanism

```

ELEMENTS
N  AR  H  O  C
END
SPECIES
N2      AR      H      O2      OH      O      H2      H2O
HO2     H2O2    CO      CO2     HCO     CH2O   CH4     CH3
T-CH2   S-CH2    C2H4    CH3O    C2H5    C2H6   CH      C2H2
C2H3    CH2CHO   C2H4O   CH2CO   HCCO    C2H    CH2OH   CH3OH
C3H4    C3H3     C3H5    C3H6    C3H8    I-C3H7 N-C3H7
END
REACTIONS
H+O2<=>OH+O          3.520e+16  -0.700  17069.79
H2+O<=>OH+H          5.060e+04  2.670   6290.63
H2+OH<=>H2O+H        1.170e+09  1.300   3635.28
H2O+O<=>2 OH         7.600e+00  3.840  12779.64
H+O+M<=>OH+M         6.200e+16  -0.600   0.00
H2/2.50/ H2O/12.00/
CO/1.90/ CO2/3.80/

H2+O2<=>2 OH         1.700e+13  0.000  47813.10
2 H+M<=>H2+M         7.200e+17  -1.000   0.00
H2/2.50/ H2O/16.30/
CO/1.90/ CO2/3.80/

H+OH+M<=>H2O+M       3.800e+22  -2.000   0.00
H2/2.50/ H2O/12.00/
CO/1.90/ CO2/3.80/

2 O+M<=>O2+M         6.170e+15  -0.500   0.00
H2/2.50/ H2O/12.00/
CO/1.90/ CO2/3.80/

H+O2 (+M) <=>HO2 (+M) 4.650e+12  0.440   0.00
AR/0.50/ O2/0.30/ H2O/7.00/
CO/0.75/ CO2/1.50/
C2H6/1.50/

      LOW / 2.600e+19  -1.200  0.00 /
      TROE/ 0 345.00  1.00 345.00 /
O+OH+M<=>HO2+M       1.000e+16  0.000   0.00

HO2+H<=>2 OH         7.080e+13  0.000   299.95
HO2+H<=>H2+O2        4.280e+13  0.000  1410.13
HO2+H<=>H2O+O        3.100e+13  0.000  1720.84
HO2+O<=>OH+O2        2.000e+13  0.000   0.00
HO2+OH<=>H2O+O2     2.890e+13  0.000  -497.13
2 OH (+M) <=>H2O2 (+M) 7.400e+13  -0.370   0.00
AR/0.70/ H2/2.00/ H2O/6.00/
CO/1.50/ CO2/2.00/ CH4/2.00/
C2H6/3.00/

      LOW / 1.340e+17  -0.584  -2294.46 /
      TROE/ 0.735  94.00  1756.00  5182.00 /
2 HO2<=>H2O2+O2      3.020e+12  0.000  1386.23
H2O2+H<=>HO2+H2      4.790e+13  0.000  7958.89
H2O2+H<=>H2O+OH      1.000e+13  0.000  3585.09
H2O2+OH<=>H2O+HO2    7.080e+12  0.000  1434.03
H2O2+O<=>HO2+OH      9.630e+06  2.000  3991.40
CO+OH<=>CO2+H        4.400e+06  1.500  -740.92

```

CO+H2O<=>CO2+OH	6.030e+13	0.000	22944.55
HCO+M<=>CO+H+M	1.860e+17	-1.000	17000.48
H2/1.90/ H2O/12.00/ CO/2.50/ CO2/2.50/			
HCO+H<=>CO+H2	1.000e+14	0.000	0.00
HCO+O<=>CO+OH	3.000e+13	0.000	0.00
HCO+O<=>CO2+H	3.000e+13	0.000	0.00
HCO+OH<=>CO+H2O	5.020e+13	0.000	0.00
HCO+O2<=>CO+H2O	3.000e+12	0.000	0.00
CH2O+M<=>HCO+H+M	6.260e+16	0.000	77915.87
H2/2.50/ H2O/16.30/ CO/1.90/ CO2/3.80/			
CH2O+H<=>HCO+H2	1.260e+08	1.620	2165.39
CH2O+O<=>HCO+OH	3.500e+13	0.000	3513.38
CH2O+OH<=>HCO+H2O	3.900e+10	0.890	406.31
CH4+H<=>H2+CH3	1.300e+04	3.000	8037.76
CH4+OH<=>H2O+CH3	1.600e+07	1.830	2782.03
CH4+O<=>CH3+OH	1.900e+09	1.440	8675.91
CH4+O2<=>CH3+HO2	3.980e+13	0.000	56890.54
CH4+HO2<=>CH3+H2O2	9.030e+12	0.000	24641.49
CH3+H<=>T-CH2+H2	1.800e+14	0.000	15105.16
CH3+H<=>S-CH2+H2	1.550e+14	0.000	13479.92
CH3+OH<=>S-CH2+H2O	1.000e+13	0.000	2502.39
CH3+O<=>CH2O+H	8.430e+13	0.000	0.00
CH3+T-CH2<=>C2H4+H	4.220e+13	0.000	0.00
CH3+HO2<=>CH3O+OH	5.000e+12	0.000	0.00
CH3+O2<=>CH2O+OH	3.300e+11	0.000	8941.20
CH3+O2<=>CH3O+O	1.330e+14	0.000	31405.35
2 CH3<=>C2H4+H2	1.000e+14	0.000	32002.87
2 CH3<=>C2H5+H	3.160e+13	0.000	14698.85
CH3+H(+M)<=>CH4(+M)	2.110e+14	0.000	0.00
LOW / 6.260e+23 -1.800 0.00 / TROE/ 0.37 3315.00 61.00 /			
2 CH3(+M)<=>C2H6(+M)	1.810e+13	0.000	0.00
LOW / 1.270e+41 -7.000 2762.91 / TROE/ 0.62 73.00 1180.00 /			
S-CH2+OH<=>CH2O+H	3.000e+13	0.000	0.00
S-CH2+O2<=>CO+OH+H	3.130e+13	0.000	0.00
S-CH2+CO2<=>CO+CH2O	3.000e+12	0.000	0.00
S-CH2+M<=>T-CH2+M	6.000e+12	0.000	0.00
H2/2.40/ H2O/15.40/ CO/1.80/ CO2/3.60/			
T-CH2+H<=>CH+H2	6.020e+12	0.000	-1787.76
T-CH2+OH<=>CH2O+H	2.500e+13	0.000	0.00
T-CH2+OH<=>CH+H2O	1.130e+07	2.000	2999.52
T-CH2+O<=>CO+2H	8.000e+13	0.000	0.00
T-CH2+O<=>CO+H2	4.000e+13	0.000	0.00
T-CH2+O2<=>CO2+H2	2.630e+12	0.000	1491.40
T-CH2+O2<=>CO+OH+H	6.580e+12	0.000	1491.40
2 T-CH2<=>C2H2+2H	1.000e+14	0.000	0.00
CH+O<=>CO+H	4.000e+13	0.000	0.00
CH+O2<=>HCO+O	1.770e+11	0.760	-478.01
CH+H2O<=>CH2O+H	1.170e+15	-0.750	0.00
CH+CO2<=>HCO+CO	4.800e+01	3.220	-3226.58
CH3O+H<=>CH2O+H2	2.000e+13	0.000	0.00
CH3O+H<=>S-CH2+H2O	1.600e+13	0.000	0.00
CH3O+OH<=>CH2O+H2O	5.000e+12	0.000	0.00
CH3O+O<=>OH+CH2O	1.000e+13	0.000	0.00
CH3O+O2<=>CH2O+HO2	4.280e-13	7.600	-3537.28
CH3O+M<=>CH2O+H+M	1.000e+13	0.000	13503.82
C2H6+H<=>C2H5+H2	5.400e+02	3.500	5210.33

C2H6+O<=>C2H5+OH	1.400e+00	4.300	2772.47
C2H6+OH<=>C2H5+H2O	2.200e+07	1.900	1123.33
C2H6+CH3<=>C2H5+CH4	5.500e-01	4.000	8293.50
C2H6 (+M) <=>C2H5+H (+M)	8.850e+20	-1.230	102222.75

LOW / 4.900e+42 -6.430 107170.17 /

TROE/ 0.84 125.00 2219.00 6882.00 /

C2H5+H<=>C2H4+H2	3.000e+13	0.000	0.00
C2H5+O<=>C2H4+OH	3.060e+13	0.000	0.00
C2H5+O<=>CH3+CH2O	4.240e+13	0.000	0.00
C2H5+O2<=>C2H4+HO2	2.000e+12	0.000	4995.22
C2H5 (+M) <=>C2H4+H (+M)	1.110e+10	1.037	36768.64

LOW / 3.990e+33 -4.990 40000.00 /

TROE/ 0.168 1203.00 0.00 /

C2H4+H<=>C2H3+H2	4.490e+07	2.120	13360.42
C2H4+OH<=>C2H3+H2O	5.530e+05	2.310	2963.67
C2H4+O<=>CH3+HCO	2.250e+06	2.080	0.00
C2H4+O<=>CH2CHO+H	1.210e+06	2.080	0.00
2 C2H4<=>C2H3+C2H5	5.010e+14	0.000	64700.05
C2H4+O2<=>C2H3+HO2	4.220e+13	0.000	57623.09
C2H4+HO2<=>C2H4O+OH	2.230e+12	0.000	17189.29
C2H4O+HO2<=>CH3+CO+H2O2	4.000e+12	0.000	17007.65
C2H4+M<=>C2H3+H+M	2.600e+17	0.000	96568.12

C2H4+M<=>C2H2+H2+M	3.500e+16	0.000	71532.03
--------------------	-----------	-------	----------

C2H3+H<=>C2H2+H2	1.210e+13	0.000	0.00
------------------	-----------	-------	------

C2H3 (+M) <=>C2H2+H (+M)	6.380e+09	1.000	37626.67
--------------------------	-----------	-------	----------

LOW / 1.510e+14 0.100 32686.42 /

TROE/ 0.3 1e+30 1e-30 /

C2H3+O2<=>CH2O+HCO	1.700e+29	-5.312	6503.11
C2H3+O2<=>CH2CHO+O	7.000e+14	-0.611	5262.43
C2H3+O2<=>C2H2+HO2	5.190e+15	-1.260	3312.62
CH2CHO<=>CH2CO+H	1.047e+37	-7.189	44340.34
C2H2+O<=>HCCO+H	4.000e+14	0.000	10659.66
C2H2+O<=>T-CH2+CO	1.600e+14	0.000	9894.84
C2H2+O2<=>CH2O+CO	4.600e+15	-0.540	44933.08
C2H2+OH<=>CH2CO+H	1.900e+07	1.700	999.04
C2H2+OH<=>C2H+H2O	3.370e+07	2.000	14000.96
CH2CO+H<=>CH3+CO	1.500e+09	1.430	2688.81
CH2CO+O<=>T-CH2+CO2	2.000e+13	0.000	2294.46
CH2CO+O<=>HCCO+OH	1.000e+13	0.000	2000.48
CH2CO+CH3<=>C2H5+CO	9.000e+10	0.000	0.00
HCCO+H<=>S-CH2+CO	1.500e+14	0.000	0.00
HCCO+OH<=>HCO+CO+H	2.000e+12	0.000	0.00
HCCO+O<=>2 CO+H	9.640e+13	0.000	0.00
HCCO+O2<=>2 CO+OH	2.880e+07	1.700	1001.43
HCCO+O2<=>CO2+CO+H	1.400e+07	1.700	1001.43
C2H+OH<=>HCCO+H	2.000e+13	0.000	0.00
C2H+O<=>CO+CH	1.020e+13	0.000	0.00
C2H+O2<=>HCCO+O	6.020e+11	0.000	0.00
C2H+O2<=>CH+CO2	4.500e+15	0.000	25095.60
C2H+O2<=>HCO+CO	2.410e+12	0.000	0.00
CH2OH+H<=>CH2O+H2	3.000e+13	0.000	0.00
CH2OH+H<=>CH3+OH	1.750e+14	0.000	2796.37
CH2OH+OH<=>CH2O+H2O	2.400e+13	0.000	0.00
CH2OH+O2<=>CH2O+HO2	5.000e+12	0.000	0.00
CH2OH+M<=>CH2O+H+M	5.000e+13	0.000	25119.50
H2/2.40/ H2O/15.40/ CO/1.80/ CO2/3.60/ CH3O+M<=>CH2OH+M	1.000e+14	0.000	19120.46
H2/2.50/ H2O/12.00/ CO/1.90/ CO2/3.80/ CH2CO+OH<=>CH2OH+CO	1.020e+13	0.000	0.00
CH3OH+OH<=>CH2OH+H2O	1.440e+06	2.000	-838.91
CH3OH+OH<=>CH3O+H2O	6.300e+06	2.000	1505.74
CH3OH+H<=>CH2OH+H2	1.640e+07	2.000	4517.21
CH3OH+H<=>CH3O+H2	3.830e+07	2.000	5855.64
CH3OH+O<=>CH2OH+OH	1.000e+13	0.000	4684.51

CH3OH+HO2<=>CH2OH+H2O2	6.200e+12	0.000	19383.37
CH3OH+O2<=>CH2OH+HO2	2.000e+13	0.000	44933.08
C3H4+O<=>C2H4+CO	2.000e+07	1.800	1000.00
CH3+C2H2<=>C3H4+H	2.560e+09	1.100	13643.88
C3H4+O<=>HCCO+CH3	7.300e+12	0.000	2250.00
C3H3+H (+M) <=>C3H4 (+M)	3.000e+13	0.000	0.00
LOW / 9.000e+15 1.000 0.00 /			
TROE/ 0.5 1e+30 1e-30 /			
C3H3+HO2<=>C3H4+O2	2.500e+12	0.000	0.00
C3H4+OH<=>C3H3+H2O	5.300e+06	2.000	2000.00
C3H3+O2<=>CH2CO+HCO	3.000e+10	0.000	2868.07
C3H4+H (+M) <=>C3H5 (+M)	4.000e+13	0.000	0.00
LOW / 3.000e+24 -2.000 0.00 /			
TROE/ 0.8 1e+30 1e-30 /			
C3H5+H<=>C3H4+H2	1.800e+13	0.000	0.00
C3H5+O2<=>C3H4+HO2	4.990e+15	-1.400	22428.06
C3H5+CH3<=>C3H4+CH4	3.000e+12	-0.320	-130.98
C2H2+CH3 (+M) <=>C3H5 (+M)	6.000e+08	0.000	0.00
LOW / 2.000e+09 1.000 0.00 /			
TROE/ 0.5 1e+30 1e-30 /			
C3H5+OH<=>C3H4+H2O	6.000e+12	0.000	0.00
C3H3+HCO<=>C3H4+CO	2.500e+13	0.000	0.00
C3H3+HO2<=>OH+CO+C2H3	8.000e+11	0.000	0.00
C3H4+O2<=>CH3+HCO+CO	4.000e+14	0.000	41826.00
C3H6+O<=>C2H5+HCO	3.500e+07	1.650	-972.75
C3H6+OH<=>C3H5+H2O	3.100e+06	2.000	-298.28
C3H6+O<=>CH2CO+CH3+H	1.200e+08	1.650	327.44
C3H6+H<=>C3H5+H2	1.700e+05	2.500	2492.83
C3H5+H (+M) <=>C3H6 (+M)	2.000e+14	0.000	0.00
AR/0.70/ H2/2.00/ H2O/6.00/			
CO/1.50/ CO2/2.00/ CH4/2.00/			
C2H6/3.00/			
LOW / 1.330e+60 -12.000 5967.97 /			
TROE/ 0.02 1097.00 1097.00 6860.00 /			
C3H5+HO2<=>C3H6+O2	2.660e+12	0.000	0.00
C3H5+HO2<=>OH+C2H3+CH2O	3.000e+12	0.000	0.00
C2H3+CH3 (+M) <=>C3H6 (+M)	2.500e+13	0.000	0.00
AR/0.70/ H2/2.00/ H2O/6.00/			
CO/1.50/ CO2/2.00/ CH4/2.00/			
C2H6/3.00/			
LOW / 4.270e+58 -11.940 9770.55 /			
TROE/ 0.175 1341.00 60000.00 10140.00 /			
C3H6+H<=>C2H4+CH3	1.600e+22	-2.390	11185.47
CH3+C2H3<=>C3H5+H	1.500e+24	-2.830	18618.55
C3H8 (+M) <=>CH3+C2H5 (+M)	1.100e+17	0.000	84392.93
LOW / 7.830e+18 0.000 64978.49 /			
TROE/ 0.76 1946.00 38.00 /			
C3H8+O2<=>I-C3H7+HO2	4.000e+13	0.000	47500.00
C3H8+O2<=>N-C3H7+HO2	4.000e+13	0.000	50932.12
C3H8+H<=>I-C3H7+H2	1.300e+06	2.400	4471.08
C3H8+H<=>N-C3H7+H2	1.330e+06	2.540	6761.47
C3H8+O<=>I-C3H7+OH	4.760e+04	2.710	2107.31
C3H8+O<=>N-C3H7+OH	1.900e+05	2.680	3718.45
C3H8+OH<=>N-C3H7+H2O	1.400e+03	2.660	527.25
C3H8+OH<=>I-C3H7+H2O	2.700e+04	2.390	393.16
C3H8+HO2<=>I-C3H7+H2O2	9.640e+03	2.600	13917.30
C3H8+HO2<=>N-C3H7+H2O2	4.760e+04	2.550	16491.40
I-C3H7+C3H8<=>N-C3H7+C3H8	8.400e-03	4.200	8675.91
C3H6+H (+M) <=>I-C3H7 (+M)	1.330e+13	0.000	1560.71
AR/0.70/ H2/2.00/ H2O/6.00/			
CO/1.50/ CO2/2.00/ CH4/2.00/			
C2H6/3.00/			
LOW / 8.700e+42 -7.500 4732.31 /			
TROE/ 1 1000.00 645.40 6844.30 /			
I-C3H7+O2<=>C3H6+HO2	1.300e+11	0.000	0.00
N-C3H7 (+M) <=>CH3+C2H4 (+M)	1.230e+13	-0.100	30210.33

```

LOW / 5.490e+49 -10.000 35779.16 /
TROE/ -1.17 251.00 0.00 1185.00 /
H+C3H6(+M)<=>N-C3H7(+M) 1.330e+13 0.000 3260.04
AR/0.70/ H2/2.00/ H2O/6.00/
CO/1.50/ CO2/2.00/ CH4/2.00/
C2H6/3.00/
LOW / 6.260e+38 -6.660 7000.48 /
TROE/ 1 1000.00 1310.00 48097.00 /
N-C3H7+O2<=>C3H6+H2O 9.000e+10 0.000 0.00
END

```

7.2 Appendix II: Lagrangian Jet Model

!!

Subroutine GaussianVelocityConversion(BB,RR,Us,Ug)

!!!!!!!!!!!!!!!!!!!!!!!!!!!!!!!!

!Returns U_g

!!!!!!!!!!!!!!!!!!!!!!!!!!!!!!!!

implicit none

!double precision :: GaussianVelocityConversion

!double precision :: GaussianSpreadConversion

double precision,intent(in) :: RR

double precision,intent(in) :: BB

double precision :: bg

double precision,intent(in) :: Us

double precision :: Pi

double precision,intent(out) :: Ug

Call GaussianSpreadConversion(BB,RR,bg)

Ug = ((BB**2-RR**2)*Us)/(bg*(RR*sqrt(Pi())+bg))

End Subroutine

!!

Subroutine GaussianSpreadConversion(BB,RR,bg)

!!!!!!!!!!!!!!!!!!!!!!!!!!!!!!!!

!Returns b_g

!!!!!!!!!!!!!!!!!!!!!!!!!!!!!!!!

implicit none

complex :: B,R,phi,lambda,kappa

double precision :: Pi

double precision,intent(in) :: RR,BB

double precision,intent(out) :: bg

R=cplx(RR)

B=cplx(BB)

phi = -24. * R ** 4. * B ** 2. * Pi() ** 2. + 24. * R ** 6. * Pi() ** 2. + 186. * Pi() * R ** 2. * B ** 4. - 372. * Pi() * R ** 4. * B ** 2. + 186. * Pi() * R ** 6. - 6. * B ** 6. + 18. * B ** 4. * R ** 2. - 18. * B ** 2. * R ** 4. + 6. * R ** 6. + 24. * R ** 4. * Pi() ** 2. * 2. ** (1. / 2.) * B ** 2. - 108. * Pi() * R ** 2. * B ** 4. * 2. ** (1. / 2.) + 216. * Pi() * R ** 4. * B ** 2. * 2. ** (1. / 2.) - 24. * R ** 6. * Pi() ** 2. * 2. ** (1. / 2.) - 108. * R ** 6. * Pi() * 2. ** (1. / 2.)

lambda = 8. * R ** 3. * Pi() ** (3. / 2.) - 36. * Pi() ** (1. / 2.) * R * B ** 2. + 36. * Pi() ** (1. / 2.) * R ** 3. + 54. * Pi() ** (1. / 2.) * R * 2. ** (1. / 2.) * B ** 2. - 54. * Pi() ** (1. / 2.) * R ** 3. * 2. ** (1. / 2.) + 6. * phi ** (1. / 2.)

kappa = -1. / 9. * Pi() * R ** 2. - 1. / 6. * B ** 2. + 1. / 6. * R ** 2.

bg = (1. / 6. * lambda ** (1. / 3.) - 6. * kappa / (lambda ** (1. / 3.)) - 2. / 3. * R * sqrt(Pi()))

End Subroutine

!!

```
Function Pi()  
implicit none  
double precision :: Pi  
Pi = 3.14159  
End Function
```

!!

```
Function RotameterFlowRate(rotameter,c,reading)  
  
!Converts rotameter reading to flow in SLPM of Nitrogen  
!type 1 rotameter is for fuel  
!type 2 rotameter is for diluent  
  
implicit none  
  
double precision :: flow, reading, RotameterFlowRate  
double precision :: P,P_std,T,T_std,R_std,R_methane,R_ethylene,CF  
integer          :: rotameter,c  
  
P      = 111.325  
P_std = 101.325  
T      = 294  
T_std = 294  
  
R_std      = 0.2968  
R_methane  = 0.5182  
R_ethylene = 0.2964  
  
If (c == 1) then  
  CF = sqrt(P*R_std*T_std / (R_methane*T*P_std))  
Else if (c == 2) then  
  CF = sqrt(P*R_std*T_std / (R_ethylene*T*P_std))  
Else  
  CF = sqrt(P*R_std*T_std / (R_std*T*P_std))  
End if  
  
If (rotameter == 1) Then  
  flow = (0.0009 * reading ** 2 + 0.1925 * reading + 0.2466)/CF  
Else  
  flow = (0.0009 * reading ** 2 + 0.1715 * reading - 0.5957)/CF  
EndIf  
  
  
If (flow < 0) Then  
  RotameterFlowRate = 0  
Else  
  RotameterFlowRate = flow  
EndIf  
  
End Function
```

!!

Subroutine Potential_Core_Length(D, U_0, U_a,x_e)

!calculates the length of the potential core

implicit none

double precision,intent(in) :: D
double precision,intent(in) :: U_0
double precision,intent(in) :: U_a
double precision,intent(out) :: x_e
double precision :: Beta_s

If (U_a > 0) Then
 x_e = D * sqrt(1. + U_a / U_0) / (Beta_s() * sqrt((1. - U_a / U_0)))
Else
 x_e = 6.2 * D
EndIf

End Subroutine

!!

Subroutine Velocity_Profile(D,U_0,U_a,R,x,U)

!returns the velocity at any given point

implicit none

double precision,intent(in) :: D,U_0,U_a,R,x
double precision,intent(out) :: U
double precision :: b_g
double precision :: x_e
double precision :: U_m
double precision :: Radial
double precision :: B

Call Potential_Core_Length(D, U_0, U_a,x_e)
Call Potential_Core_Edge(D, x_e, x, Radial)

!Centerline Velocity

If (x > x_e) Then
 Call JetSpread_th(D, U_0, U_a, x,B)
 Call GaussianSpreadConversion(B,Radial,b_g)
 Call Centerline_Velocity(D,U_0,U_a,x,U_m)

 U = U_m * Exp(-((R ** 2) / b_g**2)) + U_a

Else
 Call JetSpread_th(D, U_0, U_a, x, B)
 Call GaussianSpreadConversion(B,Radial,b_g)

 If (R > Radial) Then
 U_m = U_0 - U_a
 U = U_m * Exp(-((R - Radial) ** 2 / b_g ** 2)) + U_a
 Else
 U = U_0
 EndIf

EndIf

End Subroutine


```

    U_m=Ug+U_a
else
    U_m=U_0
endif
End Subroutine

```

!!

```

Subroutine Shear_Layer_Velocity(D, U_a, U_0, R, B, Us)

```

```

implicit none

```

```

double precision,intent(in)  :: D
double precision,intent(in)  :: U_a
double precision,intent(in)  :: U_0
double precision,intent(in)  :: R
double precision,intent(in)  :: B
double precision,intent(out) :: Us
double precision             :: C

```

```

C = ((D ** 2) - 4. * (R ** 2)) * U_0 * (U_0 - U_a) / (4. * ((B ** 2) - (R ** 2)))
Us = -U_a / 2. + (1. / 2.) * sqrt(U_a ** 2 + 4. * C)
!Write(*,*)Us
End Subroutine

```

!!

```

Subroutine Interpolate(x1, x2, x3, y1, y2, y3, x_need,y_out)

```

```

!Lagrangian Polynomial Interpolation
!-uses 3 points to interpolate the desired data point

```

```

implicit none

```

```

double precision,intent(in)  :: x1
double precision,intent(in)  :: x2
double precision,intent(in)  :: x3
double precision,intent(in)  :: y1
double precision,intent(in)  :: y2
double precision,intent(in)  :: y3
double precision,intent(in)  :: x_need
double precision,intent(out) :: y_out
integer                      :: j,k
double precision             :: P(3),x(3),y(3)

```

```

x(1) = x1
x(2) = x2
x(3) = x3
y(1) = y1
y(2) = y2
y(3) = y3

```

```

Do j = 1,3

```

```

    P(j) = 1

```

```

    Do k = 1,3

```

```

        If (k == j) Then
        Else
            P(j) = (x_need - x(k)) / (x(j) - x(k)) * P(j)
        EndIf
    End Do

End Do

y_out=0

Do j = 1,3

    y_out = y_out + P(j) * y(j)

End Do

End Subroutine

!!!!!!!!!!!!!!!!!!!!!!!!!!!!!!!!!!!!!!!!!!!!!!!!!!!!!!!!!!!!!!!!!!!!!!!!!!!!!!!!!!!!!!

Subroutine Centerline_Concentration(D, U_0, U_a, C_0, x, C_m )

!Calculates Centerline tracer mass concentration

implicit none

!double precision          :: Centerline_Concentration
double precision,intent(in) :: D
double precision,intent(in) :: U_0
double precision,intent(in) :: U_a
double precision,intent(in) :: C_0
double precision,intent(in) :: x
double precision,intent(out) :: C_m
double precision          :: U_g
double precision          :: b_g
double precision          :: A
double precision          :: Radial
double precision          :: x_e
double precision          :: B
double precision          :: Pi
double precision          :: lambda

Call Potential_Core_Length(D, U_0, U_a,x_e)
Call Potential_Core_Edge(D, x_e, x, Radial)

A = Pi() / 4. * D ** 2

if (x>x_e) then

    Call JetSpread_th(D, U_0, U_a, x, B)
    Call GaussianSpreadConversion(B,Radial,b_g)
    Call Centerline_Velocity(D, U_0, U_a, x,U_g)

    !C_m = (C_0 * U_0 * A) / (Pi() * lambda() ** 2 * b_g ** 2 * (U_a + U_g / (1. + lambda() **
2)))
    C_m = -(C_0 * U_0 * A * (1 + lambda()**2) / (lambda()**2*b_g**2*Pi()*(U_a-
U_g+U_a*lambda()**2)))
else

    C_m = C_0

endif

End Subroutine

```



```

!!!!!!!!!!!!!!!!!!!!!!!!!!!!!!!!!!!!!!!!!!!!!!!!!!!!!!!!!!!!!!!!!!!!!!!!!!!!!!!!!!!!!!

Subroutine Find_Concentration_Radial_Position(D, U_0, U_a, C_0, C_target, x, R)

implicit none

!double precision          :: Find_Concentration_Radial_Position
double precision,intent(in) :: D
double precision,intent(in) :: U_0
double precision,intent(in) :: U_a
double precision,intent(in) :: C_0
double precision,intent(in) :: C_target
double precision,intent(in) :: x
double precision,intent(out) :: R
double precision          :: x_e
double precision          :: b_g
double precision          :: Radial
double precision          :: C_m
double precision          :: B
double precision          :: lambda

If (C_target <= 0) Then
  R = 1E+20
Else
  Call Potential_Core_Length(D, U_0, U_a, x_e)
  Call Potential_Core_Edge(D, x_e, x, Radial)

  If (x > x_e) Then

    Call JetSpread_th(D, U_0, U_a, x, B)
    Call GaussianSpreadConversion(B,Radial, b_g)
    Call Centerline_Concentration(D, U_0, U_a, C_0, x, C_m)

    R = sqrt(-1.*(lambda())**2 * b_g ** 2 * log(C_target / C_m))

  Else

    Call JetSpread_th(D, U_0, U_a, x, B)
    Call GaussianSpreadConversion(B,Radial,b_g)

    C_m = C_0

    R = Radial + sqrt(-1.*(lambda())**2 * b_g ** 2 * Log(C_target / C_m))

  EndIf

EndIf

End Subroutine

```

!!

Subroutine Radial_Velocity(D, U_0, U_a, x, R, V)

!determine the radial velocity at a given point
!by solving the continuity equation

implicit none

!double precision :: Radial_Velocity
double precision,intent(in) :: D
double precision,intent(in) :: U_0
double precision,intent(in) :: U_a
double precision,intent(in) :: x
double precision,intent(in) :: R
double precision,intent(out) :: V
integer :: i,j,n
double precision :: BB
double precision :: B_th
double precision :: dr
double precision :: dz
double precision :: v_z
double precision :: v_z_dz
double precision :: multiplier
double precision :: A(2000)
double precision :: B(2000)
double precision :: C(2000)
double precision :: F(2000)
double precision :: Bnew(2000)
double precision :: Dnew(2000)
double precision :: Solution(2000)

!number of nodes
n = 2000

!integration endpoint
Call JetSpread_th(D, U_0, U_a, x, B_th)
BB = 5*B_th

!node spacing
dr = BB / (1.0*n)
dz = dr

A(1) = 0
B(1) = 1
C(1) = 0
F(1) = 0

! build matrix terms for all but last node
Do i = 2,n - 1

Call Velocity_Profile(D, U_0, U_a, (i - 1) * dr, x,v_z)
Call Velocity_Profile(D, U_0, U_a, (i - 1) * dr, x + dz,v_z_dz)

A(i + 1) = i
B(i) = 1 - i
C(i) = 0
F(i) = -(v_z_dz - v_z) / dz * (i - 1) * dr

End Do

! build matrix term for last node
i = n
Call Velocity_Profile(D, U_0, U_a, (i - 1) * dr, x, v_z)
Call Velocity_Profile(D, U_0, U_a, (i - 1) * dr, x + dz, v_z_dz)

A(i) = i
B(i) = 1 - i
C(i) = 0
F(i) = -(v_z_dz - v_z) / dz * (i - 1) * dr

```

! Begin Thomas Method

Do i = 1, n
  Bnew(i) = B(i)
  Dnew(i) = F(i)
End Do

Do i = 2,n
  multiplier = A(i) / Bnew(i - 1)
  Bnew(i) = Bnew(i) - C(i - 1) * multiplier
  Dnew(i) = Dnew(i) - Dnew(i - 1) * multiplier
End Do

Solution(n) = Dnew(n) / Bnew(n)

Do i = n - 1,1, -1
  Solution(i) = (Dnew(i) - C(i) * Solution(i + 1)) / Bnew(i)
End Do

! End Thomas Method

!Find Desired Node

i = 0

Do
  i = i + 1
  if (dr * i > R) exit
End Do

!return v_r for desired node

Call Interpolate(dr * (i - 1), dr * (i - 0), dr * (i+1), Solution(i - 1), Solution(i - 0),
Solution(i+1), R, V)
V=Solution(i)
End Subroutine

```

!!

Subroutine JetSpread_th(D, U_0, U_a, EndPoint, B_th)

!Uses RKF45 method to calculate the jet spread
!parameter at a given distance downstream

implicit none

!double precision :: JetSpread_th
double precision,intent(in) :: D
double precision,intent(in) :: U_0
double precision,intent(in) :: U_a
double precision,intent(in) :: EndPoint
double precision,intent(out) :: B_th
double precision :: h
double precision :: s
double precision :: tolerance
integer :: i
double precision :: x(500000)
double precision :: B(500000)
double precision :: e(500000)
double precision :: k(7)
double precision :: temp
double precision :: b_rk4
double precision :: b_rk5

i = 1

s = 1

x(1) = 0.0000001

B(1) = D / 2. + 0.000000001

tolerance = 0.000000001

Do

h = 0.1

Do

Call y_RK45(U_0, U_a, D, B(i), x(i), temp)

k(1) = h * temp

Call y_RK45(U_0, U_a, D, B(i) + 1. / 4. * k(1), x(i) + 1. / 4. * h, temp)

k(2) = h * temp

Call y_RK45(U_0, U_a, D, B(i) + 3. / 32. * k(1) + 9. / 32. * k(2), x(i) + 3. / 8. * h, temp)

k(3) = h * temp

Call y_RK45(U_0, U_a, D, B(i) + 1932. / 2197. * k(1) - 7200. / 2197. * k(2) + 7296. / 2197. * k(3), x(i) + 12. / 13. * h, temp)

k(4) = h * temp

Call y_RK45(U_0, U_a, D, B(i) + 439. / 216. * k(1) - 8. * k(2) + 3680. / 513. * k(3) - 845. / 4104. * k(4), x(i) + h, temp)

k(5) = h * temp

Call y_RK45(U_0, U_a, D, B(i) - 8. / 27. * k(1) + 2. * k(2) - 3544. / 2565. * k(3) + 1859. / 4104. * k(4) - 11. / 40. * k(5), x(i) + 1. / 2. * h, temp)

k(6) = h * temp

b_rk4 = 25. / 216. * k(1) + 1408. / 2565. * k(3) + 2197. / 4104. * k(4) - 1. / 5. * k(5) + B(i)

b_rk5 = 16. / 135. * k(1) + 6656. / 12825. * k(3) + 28561. / 56430. * k(4) - 9. / 50. * k(5) + 2. / 55. * k(6) + B(i)

e(i) = Abs(b_rk4 - b_rk5)

If (e(i) < tolerance) Then

x(i + 1) = x(i) + h

B(i + 1) = b_rk5

Else

h = h * tolerance / e(i)

EndIf

If (e(i) < tolerance) exit

```
End Do

    i = i + 1

    If (x(i - 1) > EndPoint) exit
End Do
    !write(*,*)B(i-1)

If (i < 4) Then
    Call Interpolate(x(i), x(i - 1), x(i - 2), B(i), B(i - 1), B(i - 2), EndPoint, B_th)

Else
    Call Interpolate(x(i - 0), x(i - 1), x(i - 2), B(i - 0), B(i - 1), B(i - 2), EndPoint,
B_th)

EndIf
! B_th=B(i-2)
! Write(*,*)B_th

End Subroutine
```

!!

```
Subroutine y_RK45(U_0, U_a, D, B, x, dBdx)
!Part of RK45 solver to compute jet spread term
implicit none
!double precision      :: y_RK45
double precision,intent(in) :: U_0
double precision,intent(in) :: U_a
double precision,intent(in) :: D
double precision,intent(in) :: B
double precision,intent(in) :: x
double precision,intent(out) :: dBdx
double precision      :: u
double precision      :: R
double precision      :: x_e
double precision      :: C
double precision      :: Beta_s

Call Potential_Core_Length(D, U_0, U_a, x_e)
Call Potential_Core_Edge(D, x_e, x,R)

Call Shear_Layer_Velocity(D, U_a, U_0, R, B, u)

dBdx = Beta_s() * u / (u + U_a)

End Subroutine
```

!!

```
Subroutine Stoi_Mole_Fractions(x,y,a,X_f,X_N,X_O)
implicit none
integer,intent(in)      :: x
integer,intent(in)      :: y
double precision,intent(in) :: a
double precision      :: b
double precision,intent(out) :: X_f
double precision,intent(out) :: X_N
double precision,intent(out) :: X_O

b = 1.0 - a

X_f = a / (a + a*(x + y/4.) + b + 3.76*a*(x + y/4.))
X_N = (b + 3.76*a*(x + y/4.)) / (a + a*(x + y/4.) + b + 3.76*a*(x + y/4.))
X_O = (a*(x + y/4.)) / (a + a*(x + y/4.) + b + 3.76*a*(x + y/4.))

End Subroutine
```

!!

Subroutine FlameSpeed(c,h,X_f_0,S_L)

implicit none

integer,intent(in) :: c,h
double precision,intent(in) :: X_f_0
double precision,intent(out) :: S_L

if (c == 1 .and. h == 4) then
S_L = 56.842*X_f_0**3 - 143.43*X_f_0**2 + 132.37*X_f_0 - 9.8941
else if (c == 2 .and. h == 4) then
S_L = 86.017*X_f_0**3 - 207.49*X_f_0**2 + 180.68*X_f_0 + 11.78
else
S_L = 0.
end if

End Subroutine

!!

Subroutine Interpolate2(x,y,n,x_need,y_out)

!Lagrangian Polynomial Interpolation

implicit none

!double precision :: Interpolate
double precision,intent(in) :: x(1000),y(1000)
integer,intent(in) :: n
double precision,intent(in) :: x_need
double precision,intent(out) :: y_out
integer :: j,k
double precision :: P(1000)

Do j = 1,n

P(j) = 1

Do k = 1,n

If (k == j) Then

Else

P(j) = (x_need - x(k)) / (x(j) - x(k)) * P(j)

EndIf

End Do

End Do

y_out=0

Do j = 1,n

y_out = y_out + P(j) * y(j)

End Do

End Subroutine